An analytic model for the collisional transport and poloidal asymmetry distribution of impurities in tokamak plasmas

Patrick Maget, Pierre Manas, Judith Frank, Timothée Nicolas, Olivier Agullo, Xavier Garbet

An analytic model for the collisional transport and poloidal asymmetry distribution of impurities in tokamak plasmas

Patrick Maget, Pierre Manas, Judith Frank[1], Timothée Nicolas[2], Olivier Agullo[1], Xavier Garbet

CEA, IRFM, F-13108 Saint Paul-lez-Durance, France.
[1] Aix-Marseille Université, CNRS, PIIM UMR 7345, 13397 Marseille Cedex 20, France.
[2] Centre de Physique Théorique, CNRS, Ecole Polytechnique, Institut Polytechnique de Paris, Route de Saclay, 91128 PALAISEAU

E-mail: `patrick.maget@cea.fr`

Abstract. The coupling between the poloidal distribution and the collisional flux of impurities can be exploited to derive a simplified analytical model covering toroidal rotation and electrostatic potential asymmetry effects, valid in the Pfirsh-Schlüter regime. This model is benchmarked with earlier works and with the drift-kinetic code NEO, which includes the full Fokker-Planck collision operator. The low computational cost of the model, compared to NEO, is particularly adapted for fast integrated simulation purposes.

1. Introduction

The transport of impurity ions (i.e. other than Deuterium and Tritium) represents a key issue in magnetic fusion research, mainly because of the radiative losses that they can induce in the plasma core. Metallic walls surrounding the plasma constitute a source of heavy and highly radiative ions that are of particular concern. Both collisional and turbulent processes impact impurity transport, and although in many cases turbulent transport is dominant [Guirlet et al., 2006, Parisot et al., 2008, Villegas et al., 2010], there is experimental evidence that collisional transport can compete and even overcome it in the plasma core where turbulence is reduced [Petrasso et al., 1986], or when it is largely reduced by a transport barrier [Efthimion et al., 1999, Pedersen et al., 2000, Rice et al., 2002, Pütterich et al., 2011], in presence of large toroidal rotation [Ida et al., 1987, Rice et al., 1997, Romanelli and Ottaviani, 1998, Angioni et al., 2014, Casson et al., 2015] or when using Ion Cyclotron Resonance Heating (ICRH) [Chan et al., 1985, Reinke et al., 2012, Kazakov et al., 2012, Bilato et al., 2014, Casson et al., 2015, Goniche et al., 2017]. These situations are

not unusual in a tokamak, and often decide on the robustness of a scenario [Tokar et al., 1995, Rapp et al., 1997, Neu et al., 2002, Fedorczak et al., 2015].

The collisional impurity flux is composed of a classical part, independent of the poloidal variation of the magnetic field amplitude, and of a neoclassical part that is due to this poloidal variation. This neoclassical component is usually larger than the classical one, by a factor $2q^2$ with q the safety factor, but it is also strongly dependent on the poloidal distribution of the impurity [Helander, 1998, Angioni and Helander, 2014]. The relation between the neoclassical flux and the poloidal asymmetry of the impurity can be formulated in a geometrical representation [Maget et al., 2020]. In this representation, the horizontal and vertical poloidal asymmetries are positioned on a circle whose characteristics depends on the plasma equilibrium, and the actual position on the circle is given by an angle depending on the collision frequency of the impurity with the main ions. The impurity flux derives directly from the resulting poloidal asymmetry, and for a given impurity profile, it can be sufficiently reduced by this asymmetry to become lower than the classical flux [Helander, 1998]. But the poloidal asymmetry changes as the impurity profile evolves to steady-state. In the simplest case (no toroidal rotation, poloidally symmetric electrostatic potential), the final impurity distribution has no asymmetry, so that the impurity peaking would be identical to the neoclassical prediction without poloidal asymmetry [Maget et al., 2020].

In the present work, we extend our analytic model to describe finite toroidal rotation (section 2), and we consider in section 3 three academic applications of interest for present fusion plasma experiments: the case of a "natural" plasma (no toroidal rotation, no ICRH heating), where we discuss the implication of a residual asymmetry of the electrostatic potential; the case of pure toroidal rotation; and the case of plasma heating at the Ion Cyclotron Resonance Frequency (ICRF) with the Hydrogen minority heating scheme. The two last situations are well known to push collisional transport at a level comparable or even above the turbulent one. Because of the strong link between the impurity gradient, the poloidal asymmetry and the flux, the impurity distribution, diffusion and pinch velocity vary during the evolution to steady state, invalidating some features of the flat profile situation, as exemplified by the "natural" case where the final impurity peaking loses any potential reduction. We benchmark our model against the drift-kinetic code NEO [Belli and Candy, 2008] for the three cases mentioned above, in the steady state regime where this code is applicable. This validation is of particular interest because of the low computational cost of the model that allows its use in fast integrated simulations. The main results are summarized in section 4.

2. Collisional impurity flux and poloidal asymmetry

The collisional impurity flux can be expressed as the sum of a neoclassical and a classical parts. The neoclassical component is generally considered as dominant, since in the absence of poloidal asymmetries it exceeds the classical part by a factor $2q^2$ with q the safety factor. But while the classical part is weakly affected by the poloidal

distribution of the impurity, the neoclassical part can be drastically reduced and can become subdominant, in particular for highly charged species [Helander, 1998]. In this section, we express these two components of the flux in the general case together with the poloidal asymmetry constraint, and then we derive the analytic model in the large aspect ratio limit.

2.1. General case

In the Pfirsh-Schlüter regime, the neoclassical flux of an impurity species "a" in presence of toroidal rotation can be expressed as (see Appendix A):

$$\begin{aligned}\left\langle \Gamma_a^{neo}\cdot\nabla\psi\right\rangle = m_a\nu_a\left\langle n_a\right\rangle\frac{F^2T_a}{e_a^2\left\langle B^2\right\rangle}\Bigg[&\left(\frac{1}{\left\langle\frac{b^2}{n}\right\rangle}-\left\langle\frac{n}{b^2}\right\rangle\right)\mathcal{G}_\psi+\left(\frac{\left\langle b^2/N\right\rangle}{\left\langle b^2/n\right\rangle}-\left\langle\frac{n}{N}\right\rangle\right)\mathcal{U}_\psi\\&+\frac{m_a\Omega^2}{2T_a}\left(1-\frac{m_i}{m_a}\frac{e_a}{e_i}\right)\left(\left\langle\frac{n\partial_\psi R^2}{b^2}\right\rangle-\frac{\left\langle\partial_\psi R^2\right\rangle}{\left\langle b^2/n\right\rangle}\right)\Bigg]\end{aligned}\tag{1}$$

where the equilibrium magnetic field is parametrized as $\mathbf{B}=F\nabla\varphi+\nabla\varphi\times\nabla\psi$ with φ the toroidal angle and ψ the poloidal magnetic flux. We note Ω the toroidal angular frequency, R is the major radius and the label "i" refers to the main ion species. In addition to toroidal rotation, the drive for the impurity flux is the impurity and main ion density and temperature gradients, that are contained in $\mathcal{G}$ and $\mathcal{U}$ as follows:

$$\mathcal{G}_\psi\equiv\partial_\psi\ln p_a-\frac{T_i}{T_a}\frac{e_a}{e_i}\partial_\psi\ln p_i+C_0^a\frac{T_i}{T_a}\frac{e_a}{e_i}\partial_\psi\ln T_i\tag{2}$$

$$\mathcal{U}_\psi\equiv u(\psi)\frac{\left\langle B^2\right\rangle}{F}\frac{e_a}{T_a}\tag{3}$$

with $C_0^a\approx 1.5$ for heavy impurities (other definitions can be found in Appendix A).

This neoclassical flux is complemented by a classical flux that can be expressed, in the limit where $\nabla\psi\cdot\nabla\theta\approx 0$, as:

$$\begin{aligned}\left\langle \Gamma_a^{cl}\cdot\nabla\psi\right\rangle \approx -\frac{m_a\nu_a\left\langle n_a\right\rangle F^2T_a}{e_a^2\left\langle B^2\right\rangle}\Bigg[&\left(\frac{\left\langle B^2\right\rangle}{F^2}\left\langle nR^2\right\rangle-\left\langle\frac{n}{b^2}\right\rangle\right)\mathcal{G}_\psi\\&-\frac{m_a\Omega^2}{2T_a}\left(1-\frac{m_i}{m_a}\frac{e_a}{e_i}\right)\left(\frac{\left\langle B^2\right\rangle}{F^2}\left\langle nR^2\partial_\psi R^2\right\rangle-\left\langle\frac{n\partial_\psi R^2}{b^2}\right\rangle\right)\Bigg]\end{aligned}\tag{4}$$

that can be further approximated as (see Appendix B):

$$\left\langle \Gamma_a^{cl}\cdot\nabla\psi\right\rangle \approx -\frac{m_a\nu_a\left\langle n_a\right\rangle F^2T_a}{e_a^2\left\langle B^2\right\rangle}\left(\frac{\epsilon}{q}\right)^2\left[\left\langle\frac{n}{b^2}\right\rangle\mathcal{G}_\psi-\frac{m_a\Omega^2}{2T_a}\left(1-\frac{m_i}{m_a}\frac{e_a}{e_i}\right)\left\langle\frac{n\partial_\psi R^2}{b^2}\right\rangle\right]\tag{5}$$

with $\epsilon=r/R$ and q the safety factor. The poloidal variation of the magnetic field, and of the impurity and main ion densities are contained respectively in b, n and N:

$$b^2=B^2/\left\langle B^2\right\rangle\tag{6}$$

$$n=n_a/\left\langle n_a\right\rangle\tag{7}$$

$$N=n_i/\left\langle n_i\right\rangle\tag{8}$$

The neoclassical impurity flux is primarily driven by the poloidal variation of the equilibrium magnetic field, but the poloidal distribution of the impurity density also

responds to this inhomogeneity and can strongly alter in return the amplitude of the flux. The poloidal distribution of the impurity can be determined from the parallel force balance (see Appendix A.3):

$$\partial_\theta \ln n_a + \frac{e_a}{T_a}\partial_\theta\phi - \frac{m_a\Omega^2}{2T_a}\partial_\theta R^2 = \mathcal{A}_\psi \left\{ \left(1 - \frac{b^2/n}{\langle b^2/n\rangle}\right)\mathcal{G}_\psi + \left(\frac{b^2}{N} - \left\langle\frac{b^2}{N}\right\rangle\frac{b^2/n}{\langle b^2/n\rangle}\right)\mathcal{U}_\psi \right. \\ \left. + \frac{m_a\Omega^2}{2T_a}\left(1 - \frac{m_i}{m_a}\frac{e_a}{e_i}\right)\left(\frac{b^2/n}{\langle b^2/n\rangle}\langle\partial_\psi R^2\rangle - \partial_\psi R^2\right)\right\} \quad (9)$$

with $\mathcal{A}_\psi = JF\, m_a\nu_a/e_a$, and J is the Jacobian of the co-ordinate system (ψ, θ, φ). It depends therefore on toroidal rotation and on the poloidal asymmetry of the electrostatic potential, but also on the friction force with the main ions.

2.2. Large aspect ratio limit

2.2.1. Radial flux The neoclassical impurity flux (equation 1) and the poloidal asymmetries (equation 9) can be both related in a simple way in the large aspect ratio limit, when retaining only the sine and cosine components of the poloidal Fourier decomposition:

$$b = 1 - \epsilon\cos\theta \quad (10)$$

$$n = 1 + \delta\cos\theta + \Delta\sin\theta \quad (11)$$

$$N = 1 + \delta_N\cos\theta + \Delta_N\sin\theta \quad (12)$$

$$\frac{e\phi}{T_e} = \frac{e\langle\phi\rangle}{T_e} + \delta_\phi\cos\theta + \Delta_\phi\sin\theta \quad (13)$$

with $\epsilon = r/R_0$ and R_0 the major radius of the magnetic axis. In the following we note $\left(\delta^a_\phi,\ \Delta^a_\phi\right) = Z_a(T_e/T_a)\left(\delta_\phi,\ \Delta_\phi\right)$. We then obtain for the impurity flux (see Appendix B):

$$\langle\Gamma^{neo}_a\cdot\nabla r\rangle \approx -\langle n_a\rangle\, D^a_{PS}\left[\left(1 + \frac{\delta}{\epsilon} + \frac{\delta^2+\Delta^2}{4\epsilon^2}\right)\mathcal{G}\right. \\ + \frac{1}{2}\left(\frac{\delta-\delta_N}{\epsilon} + \frac{\delta^2+\Delta^2-\delta\delta_N-\Delta\Delta_N}{2\epsilon^2}\right)\mathcal{U} \\ \left. - \frac{\delta_M}{2\epsilon^2 R_0}\left(1 - \frac{m_i}{m_a}\frac{e_a}{e_i}\right)\left(1 + \frac{\delta}{2\epsilon}\right)\right] \quad (14)$$

with $D^a_{PS} \equiv 2q^2 m_a\nu_a T_a/(e_a^2\langle B^2\rangle)$, $q = rB_0/\partial_r\psi$ with B_0 the magnetic field at the magnetic axis, $\delta_M = \epsilon m_a(R_0\Omega)^2/T_a$, $\mathcal{G} = (rB_0/q)\,\mathcal{G}_\psi$ and $\mathcal{U} = (rB_0/q)\,\mathcal{U}_\psi$. Note that we have also $\delta_M = 2\epsilon(m_a/m_i)(T_i/T_a)M_i^2$ with M_i the ion Mach number.

The classical heat flux can be derived in a similar way from equation (5):

$$\left\langle\Gamma^{cl}_a\cdot\nabla r\right\rangle \approx -\langle n_a\rangle\frac{D^a_{PS}}{2q^2}\left[\left(1 + \epsilon\delta + 2\epsilon^2\right)\mathcal{G} - \frac{3\delta_M}{2R_0}\left(1 - \frac{m_i}{m_a}\frac{e_a}{e_i}\right)\left(1 + \frac{\delta}{3\epsilon}\right)\right] \quad (15)$$

This flux is typically lower than the neoclassical one by a factor $\sim 2q^2$ when poloidal asymmetry is neglected. But for highly charged impurities, the neoclassical flux can be strongly reduced by poloidal asymmetries and the classical flux can then represent a larger contribution [Helander, 1998, Maget et al., 2020]. The classical flux is also less sensitive to the poloidal impurity distribution, except for the toroidal rotation term.

2.2.2. Poloidal asymmetry The equation (9) containing the constraints on the poloidal asymmetry parameters can be expressed as a system of equations relating the sine and cosine components:

$$\delta + \delta_\phi^a - \delta_M = -\mathcal{A}\left[\Delta\mathcal{G} + (\Delta - \Delta_N)\mathcal{U} - \mathcal{R}\delta_M\epsilon\Delta\right] \tag{16}$$

$$\Delta + \Delta_\phi^a = \mathcal{A}\left[(2\epsilon + \delta)\,\mathcal{G} + (\delta - \delta_N)\mathcal{U} - 2\mathcal{R}\delta_M\right] \tag{17}$$

with $\mathcal{A} = q/(rB_0)\mathcal{A}_\psi$ and

$$\mathcal{R} = \frac{1}{2r}\left(1 - \frac{m_i}{m_a}\frac{e_a}{e_i}\right) \tag{18}$$

These relations evidence the tilting of the poloidal asymmetry of the impurity due to parallel friction forces [Helander, 1998, Romanelli and Ottaviani, 1998, Fülöp and Helander, 1999].

The poloidal asymmetry parameters for the density of the impurity (δ, Δ) can be related by eliminating the collisionality parameter $\mathcal{A}$ in the system of equations (17) and (16), as was done in [Maget et al., 2020]. We introduce the following notations:

$$C_\delta^0 = -\epsilon/\left(1 + \mathcal{U}/\mathcal{G}\right) \tag{19}$$

$$\mathcal{F} = C_\delta^0\left(1 - \frac{\delta_N}{2\epsilon}\frac{\mathcal{U}}{\mathcal{G}} - \frac{\delta_M}{\epsilon}\frac{\mathcal{R}}{\mathcal{G}}\right) \tag{20}$$

$$\mathcal{H} = 1 + \delta_M C_\delta^0\frac{\mathcal{R}}{\mathcal{G}} \tag{21}$$

$$\mathcal{Q} = C_\delta^0\frac{\Delta_N}{\epsilon}\frac{\mathcal{U}}{\mathcal{G}} \tag{22}$$

so that equations (16) and (17) can be expressed as:

$$\delta + \delta_\phi^a - \delta_M = \frac{\mathcal{A}\mathcal{G}\epsilon}{C_\delta^0}\left[\Delta\mathcal{H} + \mathcal{Q}\right] \tag{23}$$

$$\Delta + \Delta_\phi^a = -\frac{\mathcal{A}\mathcal{G}\epsilon}{C_\delta^0}\left[\delta - 2\mathcal{F}\right] \tag{24}$$

This leads to

$$(\delta - C_\delta)^2 + \mathcal{H}\left(\Delta - C_\Delta\right)^2 = R_\Delta^2 \tag{25}$$

with

$$C_\delta = \mathcal{F} - \frac{\delta_\phi^a - \delta_M}{2} \tag{26}$$

$$C_\Delta = -\frac{1}{2}\left(\frac{\mathcal{Q}}{\mathcal{H}} + \Delta_\phi^a\right) \tag{27}$$

$$R_\Delta^2 = \left(\mathcal{F} + \frac{\delta_\phi^a - \delta_M}{2}\right)^2 + \frac{\mathcal{H}}{4}\left(\Delta_\phi^a - \frac{\mathcal{Q}}{\mathcal{H}}\right)^2 \tag{28}$$

The curve (δ, Δ) defined in equation (25) is an ellipsis when toroidal rotation is present ($\mathcal{H} \neq 1$) and it can be parametrized as:

$$\delta = C_\delta + R_\Delta\cos\alpha \tag{29}$$

$$\Delta = C_\Delta + R_\Delta\left(\mathcal{H}\right)^{-1/2}\sin\alpha \tag{30}$$

The collisional angle α can then be derived and we obtain:

$$\cos\alpha = \frac{R_\Delta C_\delta^0}{\mathcal{D}}\left\{\left[\left(\frac{\mathcal{A}\mathcal{G}\epsilon}{C_\delta^0}\right)^2\mathcal{H}-1\right]\left(\frac{\mathcal{F}}{C_\delta^0}+\frac{\delta_\phi^a-\delta_M}{2C_\delta^0}\right) + \frac{\mathcal{A}\mathcal{G}\epsilon}{C_\delta^0}\left[\frac{\Delta_N}{2\epsilon}\frac{\mathcal{U}}{\mathcal{G}}-\mathcal{H}\frac{\Delta_\phi^a}{2C_\delta^0}\right]\right\} \tag{31}$$

$$\sin\alpha = \frac{R_\Delta C_\delta^0}{\mathcal{D}}\mathcal{H}^{1/2}\left\{\left[\left(\frac{\mathcal{A}\mathcal{G}\epsilon}{C_\delta^0}\right)^2\mathcal{H}-1\right]\left(\frac{\Delta_\phi^a}{2C_\delta^0}-\frac{\Delta_N}{2\epsilon}\frac{\mathcal{U}}{\mathcal{G}\mathcal{H}}\right) + 2\frac{\mathcal{A}\mathcal{G}\epsilon}{C_\delta^0}\left(\frac{\mathcal{F}}{C_\delta^0}+\frac{\delta_\phi^a-\delta_M}{2C_\delta^0}\right)\right\} \tag{32}$$

with $\mathcal{D} = R_\Delta^2 + \mathcal{H}\left(\mathcal{A}\mathcal{G}\epsilon\right)^2\left(R_\Delta/C_\delta^0\right)^2$. The system of equations (26), (27), (28), (29), (30), (31), (32) fully determines the asymmetry of the impurity density as a function of its collisional friction with the main ions ($\mathcal{A}$), of the main ion and impurity gradients ($\mathcal{G}$ and $\mathcal{U}$), toroidal rotation ($\mathcal{H}$) and of the asymmetries of the main ion density (δ_N, Δ_N) and electrostatic potential (δ_ϕ, Δ_ϕ). This asymmetry gives in return the impurity flux expressed in equations (14) and (15).

3. Applications

In this section, we illustrate the potential applications of the analytic model by considering first the "natural" case, and then two situations where the neoclassical transport of impurities can compete with turbulent processes: toroidal rotation and Ion Cyclotron Resonance Heating, in the core region. For this, we need to determine the asymmetries of the main ion density and electrostatic potential. We consider a Boltzmann distribution of both electrons and main ions, and this leads to an electrostatic potential that has a horizontal asymmetry driven by the anisotropic temperature of the minority ions and by toroidal rotation [Kazakov et al., 2012, Reinke et al., 2012]:

$$\delta_\phi = \frac{\epsilon}{1+Z_iT_e/T_i}\left[f_H\left(\frac{T_\perp}{T_\parallel}-1\right)\frac{b_C}{b_C+\frac{T_\perp}{T_\parallel}\left(1-b_C\right)}+m_i\frac{\left(R_0\Omega\right)^2}{T_i}\right] \tag{33}$$

with f_H the Hydrogen minority fraction and $b_C = B^{res}/B_0$ and B^{res} the magnetic field where the ICRH frequency matches the fundamental cyclotron resonance of the minority ion.

In addition to this horizontal asymmetry driven by rotation and ICRF heating, a small residual asymmetry of the electrostatic potential is spontaneously driven by collisions and by turbulence, and this residual is particularly important in the "natural" case. In the purely collisional case, this asymmetry is essentially vertical [Hinton and Rosenbluth, 1973], as found with PIC simulations [Dominski et al., 2019] and with NEO [Belli and Candy, 2008]. An analytic derivation by Wong et al [Wong and Chan, 2009] will be used here. It exhibits a sharp discontinuity at $\theta = \pm\pi$

that is expected to be smoothed by collisions, and a simplified expression for the natural Δ_ϕ can be derived from this work:

$$\Delta_\phi^{nat} \approx \frac{C^{nat.}}{Z_i + T_e/T_i} \frac{q^2 x}{\epsilon^{5/2}} \frac{\partial_x \ln T_i}{\tau_{ii}\Omega_i} \tag{34}$$

with $C^{nat} \approx -0.165$ and $\Omega_i \equiv e_i B_0/m_i$. The electrostatic potential asymmetry driven by turbulence, which will not be discussed here, is not purely vertical following GYSELA simulations by Estève et al [Estève et al., 2018] since an horizontal component, driven by the ballooning of the turbulence Reynolds stress, is also generated [Donnel et al., 2018]. This asymmetry of the electrostatic potential, combined with the turbulence driven asymmetry of the pressure tensor of the impurity, have been shown to influence the poloidal distribution of the impurity [Donnel et al., 2019]. In situations where the collisional transport of the impurity is dominant over its turbulent part, the weight of these underlying asymmetries remains an interesting open issue.

For the poloidal variation of the main ion density, we get from the parallel force balance without collisions (equation 9):

$$n_i = \langle n_i \rangle \exp\left(-\frac{e_i \phi}{T_i} + \frac{m_i \Omega^2}{2T_i} \left(R^2 - \langle R^2 \rangle \right) \right) \tag{35}$$

which gives :

$$\delta_N = -Z_i \frac{T_e}{T_i} \delta_\phi + \frac{\epsilon m_i (R_0 \Omega)^2}{T_i} \tag{36}$$

$$\Delta_N = -Z_i \frac{T_e}{T_i} \Delta_\phi \tag{37}$$

The parameter $\mathcal{U}$ can be expressed in a simple way after considering the fact that neoclassical friction constrains the poloidal flow. This gives (see [Maget et al., 2020]):

$$u(\psi) \approx -\frac{C_0^a + k_i}{\langle B^2 \rangle} \frac{T_i}{e_i} \frac{q}{\epsilon} \partial_r \ln T_i \tag{38}$$

with k_i a neoclassical friction coefficient that tends asymptotically to -1.17 in the banana regime. This coefficient as well as the collision frequency ν_a are computed following the model described in Kessel [Kessel, 1994].

We consider geometrical parameters typical for the WEST tokamak [Bourdelle et al., 2015] with inverse aspect ratio $a/R_0 = 0.2$, $B_0 = 3.7$ T, $R_0 = 2.5$ m. Equilibrium profiles are defined as:

$$q = 1 + (q_a - 1)x^2 \tag{39}$$

$$T_i = T_i^0 (1 - x^2)^2 \tag{40}$$

$$n_i = n_i^0 (1 - x^2) \tag{41}$$

with $x = r/a$, $T_i/T_e = 0.5$, $q_a = 4$, $T_e^0 = 3$ keV and $n_i^0 = 4 \times 10^{19}$ m^{-3}.

We show in figure 1 the profiles of the neoclassical coefficient k_i and of the normalized collisionality $\nu_{ji}^* = Rq/\left(\epsilon^{3/2} \tau_{ji} v_{Ti}\right)$, with $v_{Ti} = (2T_i/m_i)^{1/2}$ and

$$\tau_{ji} = \frac{3\pi^{3/2} \epsilon_0^2 m_j^2 v_{Ti}^3}{e_i^2 e_j^2 n_i \ln \Lambda_{ji}} \tag{42}$$

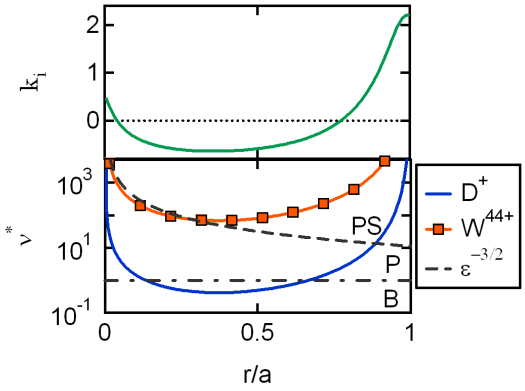

Figure 1. Neoclassical coefficient k_i (top) and collisionality regimes for the main ion species D^+, W^{44+} (bottom) as a function of the plasma radius. The collisionality domains are labelled by 'B' for the banana regime, 'P' for the plateau regime and 'PS' for the Pfirsh-Schlüter regime.

The Coulomb logarithm $\ln\Lambda_{ji}$ is taken from the NRL formulary. The banana regime corresponds to $\nu^* < 1$ and the Pfirsh-Schlüter regime to $\nu^* > \epsilon^{-3/2}$. The plateau regime is in between. We see that the main ions are marginally in the banana regime and this causes k_i to be larger than -1. The ionization state of Tungsten that we will consider in the following, W^{44+}, is close to the boundary between the plateau and Pfirsh-Schlüter regimes in the plasma core ($r/a < 0.5$), and in the Pfirsh-Schlüter regime in the outer part of the plasma.

The pinch velocity and poloidal asymmetry derived from our model will be compared with the Fülöp-Helander model [Helander, 1998, Fülöp and Helander, 1999]. The pinch velocity of the impurity given in eq. (36) of [Fülöp and Helander, 1999] can be expressed with our notations as:

$$V_{r,a}^{FH} = -\frac{Z_i}{Z_a}\frac{T_a}{eB_0R_0q^2}\mathcal{A}\mathcal{G}_0\epsilon\left\{1+\left(1+M_0^2\right)\left(1-\frac{\epsilon M_0^2}{C_\delta^0}\right)\frac{2q^2(C_\delta^0)^2}{\left(\mathcal{A}\mathcal{G}_0\epsilon\right)^2+(C_\delta^0)^2}\right\} \tag{43}$$

with

$$M_0^2 = \frac{\delta_M}{2\epsilon}\left(1-Z_a\frac{m_i}{m_a}\frac{T_e}{T_e+T_i}\right) \tag{44}$$

Here $\mathcal{G}_0$ corresponds to $\mathcal{G}$ without the impurity pressure gradient. The latter is not present in this model because the diamagnetic rotation of the impurity, considered as small compared with the $\mathbf{E}\times\mathbf{B}$ rotation, is neglected. The asymmetry is expressed in this model as :

$$\delta^{FH} = 2C_\delta^0\frac{\left(\mathcal{A}\mathcal{G}_0\epsilon\right)^2+\epsilon C_\delta^0M_0^2}{\left(\mathcal{A}\mathcal{G}_0\epsilon\right)^2+(C_\delta^0)^2} \tag{45}$$

$$\Delta^{FH} = 2\mathcal{A}\mathcal{G}_0\epsilon\frac{(C_\delta^0)^2-\epsilon C_\delta^0M_0^2}{\left(\mathcal{A}\mathcal{G}_0\epsilon\right)^2+(C_\delta^0)^2} \tag{46}$$

$$M_0^2 = \frac{\delta_M}{2\epsilon}\left(1 - Z_a\frac{m_i}{m_a}\frac{T_e}{T_e+T_i}\right) \tag{47}$$

This can be expressed in a geometrical representation as:

$$C_\delta^{FH} = C_\delta^0 + \epsilon M_0^2 \tag{48}$$

$$C_\Delta^{FH} = 0 \tag{49}$$

$$R_\Delta^{FH} = \left|C_\delta^0 - \epsilon M_0^2\right| \tag{50}$$

$$\cos\alpha^{FH} = sign\left(C_\delta^0 - \epsilon M_0^2\right)\frac{\left(\mathcal{A}\mathcal{G}_0\epsilon\right)^2 - (C_\delta^0)^2}{\left(\mathcal{A}\mathcal{G}_0\epsilon\right)^2 + (C_\delta^0)^2} \tag{51}$$

$$\sin\alpha^{FH} = sign\left(C_\delta^0 - \epsilon M_0^2\right)\frac{2\left(\mathcal{A}\mathcal{G}_0\epsilon\right)C_\delta^0}{\left(\mathcal{A}\mathcal{G}_0\epsilon\right)^2 + (C_\delta^0)^2} \tag{52}$$

We will also compare our results with computations done with the NEO code [Belli and Candy, 2008], where the steady state neoclassical diffusion and pinch velocity are determined, together with the poloidal distribution of the impurity. Computations are performed using the full Fokker-Planck collision operator with 5 Laguerre and 17 Legendre polynomials.

3.1. The "natural" case

We consider first the situation where there is no toroidal rotation and no ICRF heating. In this case, if we assume that the electrostatic potential has no asymmetry, the neoclassical pinch can be strongly reduced by the self-consistent poloidal asymmetry when the impurity profile is flat [Helander, 1998]. This is illustrated in figure 2 (left plots) where the profiles of the classical ("cl."), neoclassical ("neo"), neoclassical without poloidal asymmetry ("neo.(0)") and total ("tot.") pinch velocities are shown, together with the asymmetry parameters (δ, Δ).

However, given the low amplitude of the poloidal asymmetry and the sensitivity of the flux on its amplitude, any residual asymmetry of the electrostatic potential can be instrumental in determining the impurity flux. The amplitude of the vertical asymmetry derived from equation (34), shown in the top plot of figure 5 for the plasma parameters considered here, is small in the plasma center but can reach several percents in the edge region. If we use this expression in the analytic model, we find a drastic change in the neoclassical pinch velocity: it becomes inward instead of outward, and much larger than the pinch evaluated at $\Delta_\phi = 0$ (figure 2, right plots).

The sensitivity of the impurity distribution on the poloidal asymmetry of the electrostatic potential is outlined in figure 3, where we show the contours of the diffusion coefficient, pinch velocity, the horizontal and vertical asymmetries in the (δ_ϕ, Δ_ϕ) plane at $r/a = 0.2$ for a flat impurity profile (left column) and at steady-state, i.e. when by changing the impurity gradient, the total collisional flux, classical plus neoclassical, cancels (right column). The pinch velocity and diffusion coefficients show a nearly parabolic variation with respect to both δ_ϕ and Δ_ϕ. Notice that in this representation minority ICRF heating ($T_\perp/T_\parallel > 1$) means a positive δ_ϕ.

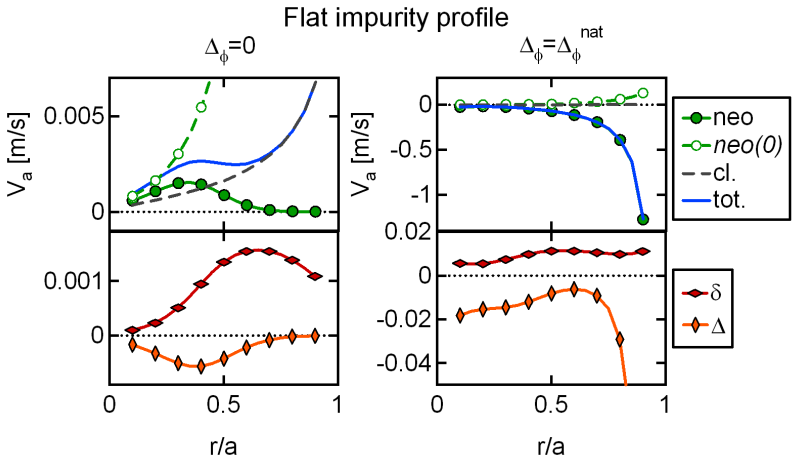

Figure 2. Natural case: profiles of the components of the pinch velocity classical ("cl."), neoclassical ("neo"), neoclassical without poloidal asymmetry ("neo.(0)") and total ("tot.") (top plots), and poloidal asymmetry parameters (δ, Δ) (bottom plots) in a situation without (left plots) and with (right plots) the natural asymmetry of the electric potential determined from equation (34).

The steady state is also strongly impacted by the asymmetry of the electrostatic potential. As shown in the right plots of figure 3, the pinch velocity and diffusion coefficient keep having a nearly parabolic variation in the (δ_ϕ, Δ_ϕ) plane. In the absence of any source of horizontal asymmetry, the steady state value of δ is close to zero but the vertical asymmetry reflects the amplitude of Δ_ϕ^{nat}, with an opposite sign. The consequence in terms of steady state impurity peaking (i.e. $\partial_x \ln n_a$) is shown in figure 4 for W^{44+} at $r/a = 0.2$ and $r/a = 0.4$, where we find again a strong sensitivity with respect to the natural vertical asymmetry Δ_ϕ^{nat}. It is interesting to note that the favourable region at $\Delta_\phi < 0$ cannot be accessed by reversing the sign of the magnetic field, which reverses the sign of Δ_ϕ^{nat}: by doing so, all the diagrams of figure 3 are reversed as well with respect to $\Delta_\phi = 0$, and the area with the most hollow steady state impurity profile in figure 4 remains out of reach. It is worth recalling however that turbulence may impose a different asymmetry for the electrostatic potential.

The "natural" case is now addressed with the NEO code. The vertical asymmetry of the electrostatic potential predicted by NEO is sinusoidal and agrees well with the formula of equation (34), as shown in figure 5 (top plot). The profiles of the steady state pinch velocity, diffusion coefficient, asymmetry parameters and impurity peaking found with the analytic model with and without Δ_ϕ^{nat} are shown in figure 5, and compared with the results from NEO. In the plasma core ($r/a < 0.4$) a reasonable agreement is found, with a Tungsten peaking that is becoming negative due to the natural vertical asymmetry. For $r/a > 0.4$, the neoclassical flux cancels only at large negative peaking factors and the steady state solution found by the model departs from the NEO result. Although a variation of the vertical asymmetry Δ_ϕ^{nat} by 50% has a large impact on the impurity distribution, as shown in the figure, the predictions of the model are

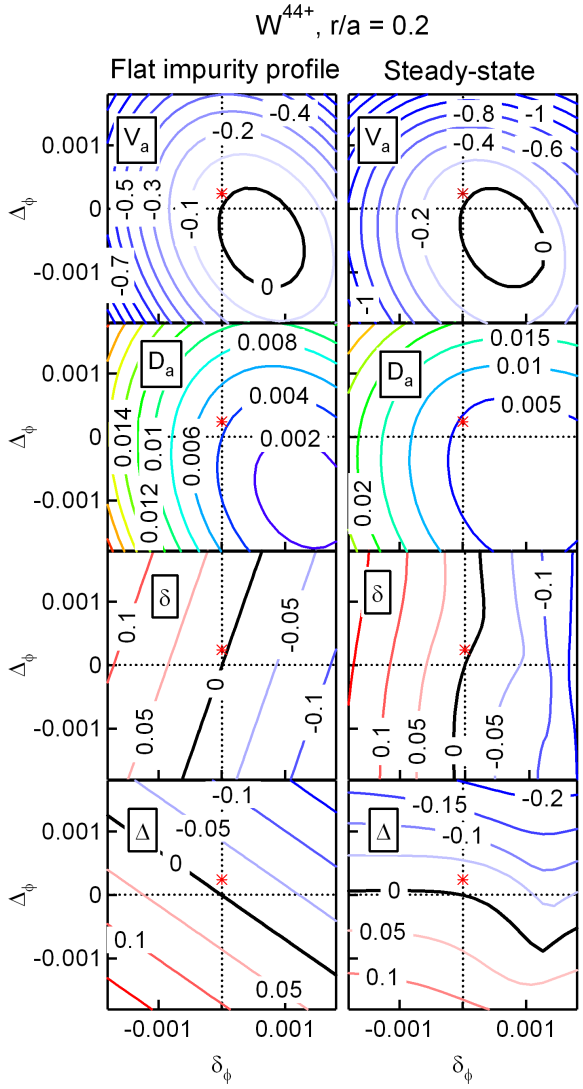

Figure 3. From top to bottom: contours of the pinch velocity, diffusion coefficient, horizontal and vertical asymmetries for W^{44+} at $r/a = 0.2$ for a flat impurity profile (left) and at steady state (right), in the $(\delta_\phi, \Delta_\phi)$ plane. The natural asymmetry of the electrostatic potential given by equation (34) is shown with a red star.

inconsistent with the solution found by NEO as Δ_ϕ^{nat} is becoming large. The reason is that the purely vertical asymmetry Δ_ϕ^{nat} induces a distortion of the steady state poloidal asymmetry of the impurity that includes an horizontal component. This is visible in figure 3 ($r/a = 0.2$), and it is more pronounced at larger radius where Δ_ϕ^{nat} and the friction force become larger. In contrast, the NEO computation does not show such an horizontal component: the asymmetry of the impurity only reflects that of the electrostatic potential (only vertical asymmetry), and does not recover the tilting due to the friction force from equation (9).

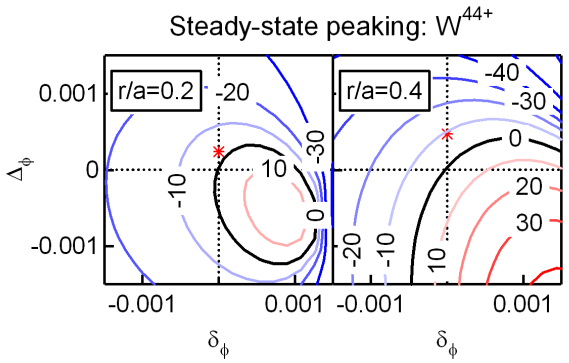

Figure 4. Steady-state peaking ($\equiv \partial_x \ln n_a$) of W^{44+} in the $(\delta_\phi, \Delta_\phi)$ plane at $r/a = 0.2$ and $r/a = 0.4$. The natural asymmetry of the electrostatic potential as given by equation (34) is shown with a red star.

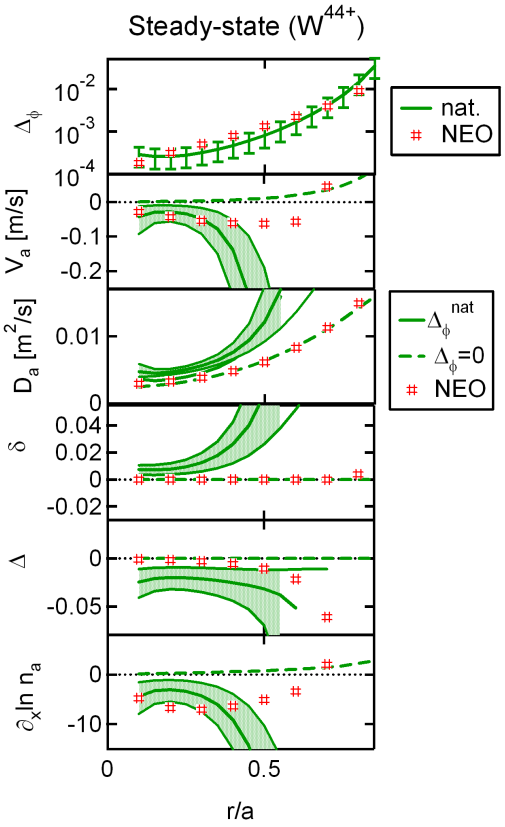

Figure 5. From top to bottom: vertical asymmetry of the electrostatic potential, pinch velocity, diffusion coefficient, horizontal and vertical asymmetry and peaking factor ($\partial_x \ln n_a$) for W^{44+} with and without the natural vertical asymmetry of the electrostatic potential, as a function of the minor radius. The shaded area indicates the variation of these parameters when Δ_ϕ^{nat} is varied by 50%. Results from NEO are shown with hastags.

3.2. Effect of toroidal rotation

3.2.1. Pinch velocity and poloidal asymmetry We first consider the case of a flat impurity profile. This allows, in the case of toroidal rotation, a comparison with the Fülöp-Helander model that does not address the steady state solution. A scan in the ion Mach number is performed for W^{44+} at $r/a = 0.2$, a region of the plasma where neoclassical transport can easily overcome turbulent transport. We show in figure 6 the pinch velocity, diffusion coefficient, and the asymmetry parameters (δ, Δ) as a function of M_i. Toroidal rotation is shown to drive a strong inward pinch, as well as a large diffusion coefficient. The horizontal asymmetry becomes positive as a result of the centrifugal force, but the vertical asymmetry is also significant, although with a lower amplitude. The pinch velocity and the poloidal asymmetry predicted by the Fülöp-Helander model are in excellent agreement. We also display for comparison the result of NEO calculations, that corresponds to the steady-state, in the same figure 6. We will discuss later (section 3.2.2) the evolution of these parameters with the impurity gradient, but we can notice here the relatively good match of the pinch and diffusion coefficient for $M_i < 0.3$ despite the imperfect match of the poloidal asymmetry, in particular its vertical component. We also note that the discrepancies on the predictions of the pinch velocity between the model and NEO at large mach numbers are also observed in [Belli et al., 2014].

We can also illustrate the evolution of the poloidal asymmetry using a geometrical representation, as shown in figure 7. A larger Mach number translates into an ellipsis with larger dimensions. We note that the circle moves away from the symmetric point (δ, Δ) = (0, 0) in the direction of larger δ as the ion Mach number increases, a feature that is not captured by the Fülöp-Helander model. This gap is precisely $2\mathcal{F}$ and increases with toroidal rotation (see equation 20), while it is simply $2C_\delta^0 \approx 6 \times 10^{-4}$ in the Fülöp-Helander model.

This can lead to a discrepancy in the horizontal asymmetry prediction between the two models for a large value of $\mathcal{AG}$ (highly charged impurities, low ion temperature or large gradients). As an example we show in figure 8 the asymmetry reconstruction for $T_i/T_e = 0.2$ instead of 0.5. The collisional angle α being close to 180^o, the vertical asymmetry is comparable for the two models, while the difference in the predicted horizontal asymmetry is large.

The figure 7 also shows that, as the ion Mach number is increased, the asymmetry parameters follow a trajectory that is quasi linear. It is in fact exactly linear in the Fülöp-Helander model since we have

$$\Delta^{FH} = \left(\delta^{FH} - C_\delta^{FH}\right) \frac{2\left(\mathcal{AG}_0\epsilon\right) C_\delta^0}{\left(\mathcal{AG}_0\epsilon\right)^2 - \left(C_\delta^0\right)^2} \tag{53}$$

where the toroidal rotation effect is contained in C_δ^{FH}. For the model derived here, we also have a linear relation for $\Delta_N = \Delta_\phi = 0$, provided $\mathcal{H} \approx 1$ since we then have:

$$\Delta = \left(\delta - C_\delta\right) \frac{2\left(\mathcal{AG}\epsilon\right) C_\delta^0}{\left(\mathcal{AG}\epsilon\right)^2 \mathcal{H} - \left(C_\delta^0\right)^2} \tag{54}$$

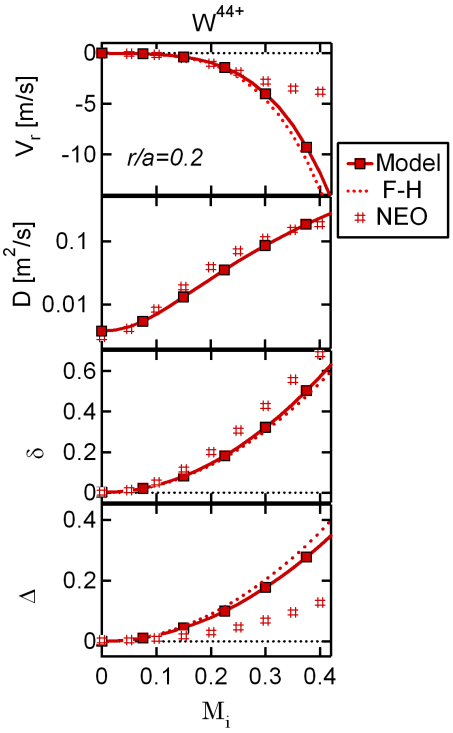

Figure 6. From top to bottom: pinch velocity, diffusion coefficient, horizontal and vertical asymmetries for a flat distribution of W^{44+} at $r/a = 0.2$, as a function of the ion Mach number. Dotted lines correspond to the Fülöp-Helander model (F-H) and hashtags to NEO (steady state) results.

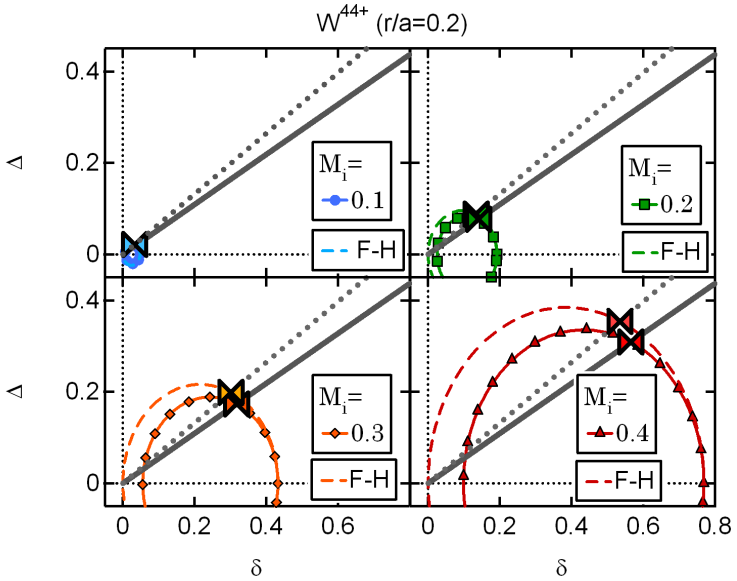

Figure 7. Geometrical representation of the elliptic curves (δ, Δ) for different values of the ion Mach number, and actual positions for W^{44+} at $r/a = 0.4$ ($\bowtie$). The prediction from the Fülöp-Helander model are shown with dashed lines.

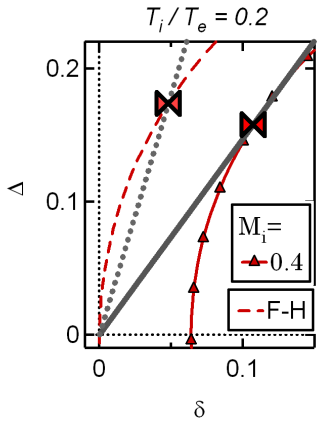

Figure 8. Geometrical representation of the elliptic curves (δ, Δ) for $M_i = 0.4$ and $T_i/T_e = 0.2$, and actual positions for W^{44+} at $r/a = 0.2$ ($\bowtie$). The prediction from the Fülöp-Helander model are shown with dashed lines.

.

3.2.2. Steady-state impurity profile The steady-state solution for the impurity density profile is obtained by cancelling the collisional flux, both classical and neoclassical when varying the impurity gradient. We assume indeed that the impurity is at a trace level, so that its impact on the main ion and electron fluxes is neglected. In the analytic model, both the pinch velocity and the diffusion coefficient are dependent on the impurity gradient through the asymmetry parameters. In NEO, these coefficients do not depend on the impurity gradient (trace limit), so that the impurity peaking can be simply deduced from $\partial_r \ln n_a = V_a/D_a$ with V_a and D_a the pinch velocity and diffusion coefficient respectively.

The impurity peaking at $r/a = 0.2$ is shown as a function of the ion Mach number in figure 9 for W^{44+}. The core accumulation of the charged impurity ions is rapidly growing and tends to saturate above $M_i \sim 0.2$. The poloidal asymmetry at steady state is characterized by a large accumulation on the low field side of the plasma, with an horizontal asymmetry that increases with M_i, while the vertical asymmetry is nearly zero. When the natural vertical asymmetry of the electrostatic potential is added, the peaking at low rotation is moving towards more negative values, but the solution at $M_i > 0.1$ is not affected, apart from the steady state vertical asymmetry that has a small remaining negative value. The agreement with NEO is reasonably good for Tungsten diffusion and pinch velocity, as well as for the horizontal asymmetry, up to $M_i \sim 0.3$. At low Mach number, taking into account the natural vertical asymmetry of the electrostatic potential improves the matching, with a Tungsten peaking that remains negative as $M_i \to 0$. For toroidal rotation larger than $M_i \sim 0.3$, the horizontal asymmetry approaches 100% and cannot be fitted accurately with (δ, Δ). The comparison with figure 6 outlines the dependence of the poloidal asymmetry on the impurity profile since the horizontal asymmetry from the model and from NEO are

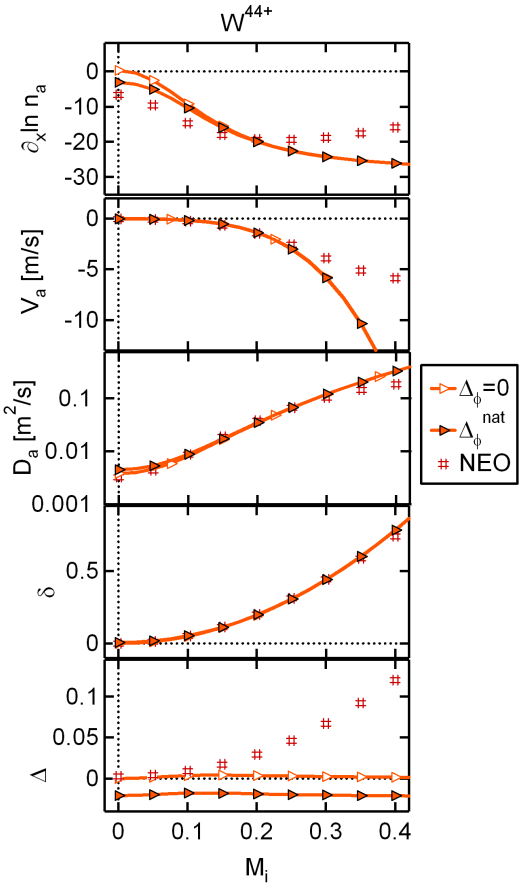

Figure 9. From top to bottom: Steady-state impurity peaking, pinch velocity, diffusion coefficient, horizontal and vertical asymmetries at $r/a = 0.2$ for W^{44+}, with $\Delta_\phi = 0$ and $\Delta_\phi = \Delta_\phi^{nat}$. The results from NEO are shown with hashtags symbols.

now in perfect agreement. The vertical asymmetry vanishes almost exactly following the model predictions with $\Delta_\phi = 0$, while the fit of $n_a(\theta)/\langle n_a \rangle$ from NEO still identifies a small remaining positive contribution.

The details of the variation of the radial velocity and poloidal asymmetry with the impurity peaking is shown in figure 10 for W^{44+}. Toroidal rotation strongly enhances the inward neoclassical impurity pinch so that the weight of the classical flux is negligible above $M_i = 0.1$. This figure also illustrates the variation of the poloidal asymmetry with the impurity peaking. The horizontal asymmetry is increasing as impurity peaking is evolving from zero to steady state, while the vertical asymmetry practically vanishes when assuming $\Delta_\phi = 0$.

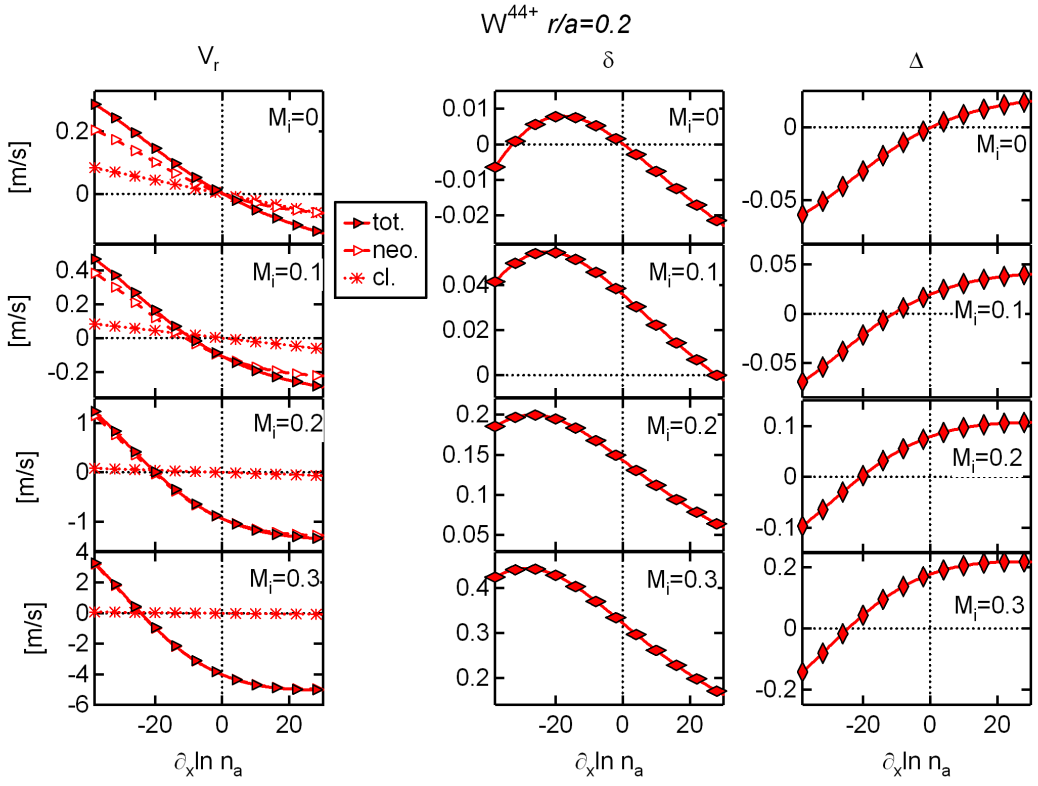

Figure 10. Total, neoclassical and classical impurity flow (left), horizontal (middle) and vertical (right) asymmetry, as a function of the impurity peaking for different values of the ion Mach number, for W^{44+} at $r/a = 0.2$ ($\Delta_\phi = 0$).

3.3. Effect of anisotropic minority ion temperature

We now consider the case of ICRH-driven temperature anisotropy, with 10% of Hydrogen minority, and a profile of the anisotropic temperature centered on the plasma core:

$$\frac{T_\perp}{T_\parallel} = 1 + \left[\left(\frac{T_\perp}{T_\parallel}\right)_0 - 1\right] \exp\left(-(x/\sigma_x)^2\right) \tag{55}$$

with $(T_\perp/T_\parallel)_0$ ranging from 1 to 5, and $\sigma_x = 0.3$. The scan is extended to $(T_\perp/T_\parallel)_0 \in [0, 1]$, a range that is not relevant for ICRH but connects with the figures of section 3.1. Formula (55) is used in equation (33) to compute the horizontal asymmetry of the electrostatic potential. The dependence of the velocity pinch, diffusion coefficient and asymmetry parameters on $(T_\perp/T_\parallel)_0$ is shown in figure 11 for a flat impurity profile. The horizontal asymmetry is driven negative by a dominant perpendicular minority temperature, as observed experimentally [Ingesson et al., 2000, Reinke et al., 2012, Bilato et al., 2014, Bilato et al., 2017, Goniche et al., 2017], and it opposes the consequence of toroidal rotation. At the same time, the pinch velocity follows a nearly parabolic curve: it moves to the outward direction first, and then becomes more inward again. This reversal of the flux is obtained with a moderate level of electrostatic potential anisotropy for Tungsten due to its large electric charge (see also

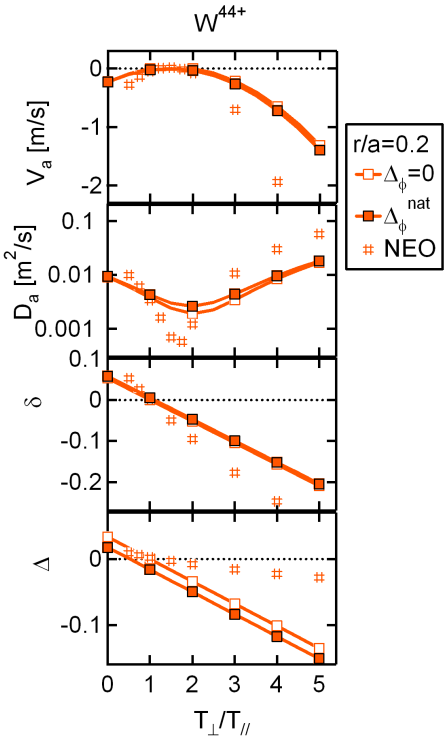

Figure 11. From top to bottom: Pinch velocity, diffusion coefficient, horizontal and vertical asymmetries for a flat profile of W^{44+} at $r/a = 0.2$, as a function of the Hydrogen temperature anisotropy. Results from the code NEO (steady state) are shown for comparison.

figure 3 of [Maget et al., 2020]). The computation has been done for $\Delta_\phi = 0$ but also for $\Delta_\phi = \Delta_\phi^{nat}$, where we assume for simplicity that this imposed vertical asymmetry of the electrostatic potential does not impact the poloidal distribution of the minority ions. The impact is limited to a shift in the vertical asymmetry of the impurity and a change of the pinch and diffusion at low $(T_\perp/T_\parallel)_0$ that will appear more clearly when computing the steady state peaking. We anticipate the discussion on the steady-state impurity profile by showing on the same plot the results obtained with the NEO code (hashtags symbols in figure 11). The pinch velocity predicted by NEO is close to the one found by the model up to $(T_\perp/T_\parallel)_0 \approx 2$, but both the diffusion coefficient and pinch velocity become much larger above that value, although they follow qualitatively the same trend. The mismatch on the horizontal asymmetry is moderate but it is large on the vertical asymmetry. We will see that these discrepancies on the poloidal distribution are much smaller in the steady state (see section 3.3.1), showing the importance of the coupling between the poloidal asymmetry and the flux during transients.

3.3.1. Steady-state impurity distribution in the case of anisotropic minority ion temperature We show in figure 12 the steady state value of the density peaking of W^{44+} at $r/a = 0.2$, as a function of $(T_\perp/T_\parallel)_0$. We find that except in a limited range of

$T_\perp/T_\parallel$ values just above unity, the asymmetry of the electrostatic potential induced by ICRH leads to impurity accumulation in the core. The region around $(T_\perp/T_\parallel)_0 \sim 2$ is particular. Indeed, the neoclassical diffusion coefficient is vanishing around $(T_\perp/T_\parallel)_0 \sim 2$ so that the neoclassical flux cannot be cancelled by changing the impurity gradient. This gives a divergence in the Tungsten peaking (labelled as 'neo' in the top plot) when cancelling its pure neoclassical component. The contribution of the classical flux is then essential. The horizontal asymmetry at steady state is decreasing quasi-linearly with $T_\perp/T_\parallel$, being positive for $T_\perp/T_\parallel < 1$ and negative for $T_\perp/T_\parallel > 1$. The vertical asymmetry is slightly negative with a minimum of a few percents for $T_\perp/T_\parallel$ between 2 and 4, and goes back towards zero as $T_\perp/T_\parallel$ increases further. Computations with NEO show a reasonable agreement, with a comparable impurity peaking. In particular, the positive peaking (hollow impurity profile) for $T_\perp/T_\parallel$ just above unity is also found. In contrast with the transient case with a flat impurity profile (see figure 11), the horizontal asymmetry agrees very well between the model and NEO. The vertical asymmetry is small and negative in the two cases. The steady state characteristics are weakly dependent on the natural vertical asymmetry of the electrostatic potential, also shown in the figure.

The variation of the collisional flux and poloidal asymmetry of W^{44+} with the impurity gradient is detailed in figure 13 for increasing temperature anisotropy. For $T_\perp/T_\parallel \sim 2$, the neoclassical flux is small and nearly independent from the impurity gradient, which gives particular importance to the classical flux, as mentioned earlier. The figure also shows that the variation of the asymmetry with the impurity peaking can be relatively large, as evidenced also by the comparison between figures 11 and 12.

The result that ICRH can lead to Tungsten accumulation seems to contradict experimental analyses where on the contrary ICRH was found to be beneficial for impurity removal from the core plasma [Valisa et al., 2011, Casson et al., 2015, Goniche et al., 2017]. In these experimental cases however, several additional effects should be considered. First, ICRH provides ion heating, which induces both an increased thermal screening effect and a change in the turbulent transport properties, that are both absent from our analysis. Second, the friction of the impurity with the minority species provides an additional screening effect that is not considered here (temperature and density gradients for the fast ions were not considered) [Casson et al., 2015, Goniche et al., 2017]. Moreover, these experimental results were also obtained in a situation where ICRH was combined with toroidal rotation. And the variation of horizontal asymmetry induced by ICRH opposes that due to toroidal rotation, thus reducing the steady state Tungsten peaking. This issue is illustrated in figure 14 where we scan both the ion Mach number and the ratio $T_\perp/T_\parallel$ to determine the steady state peaking of W^{44+} at $r/a = 0.2$, together with the poloidal asymmetry parameters. The favourable window in $T_\perp/T_\parallel$ where Tungsten is expelled moves to higher values as toroidal rotation is increased. At finite ion Mach number, increasing the minority ion temperature anisotropy leads in the first place to a reduction of impurity accumulation, consistent with experimental observations. Increasing $T_\perp/T_\parallel$ above the

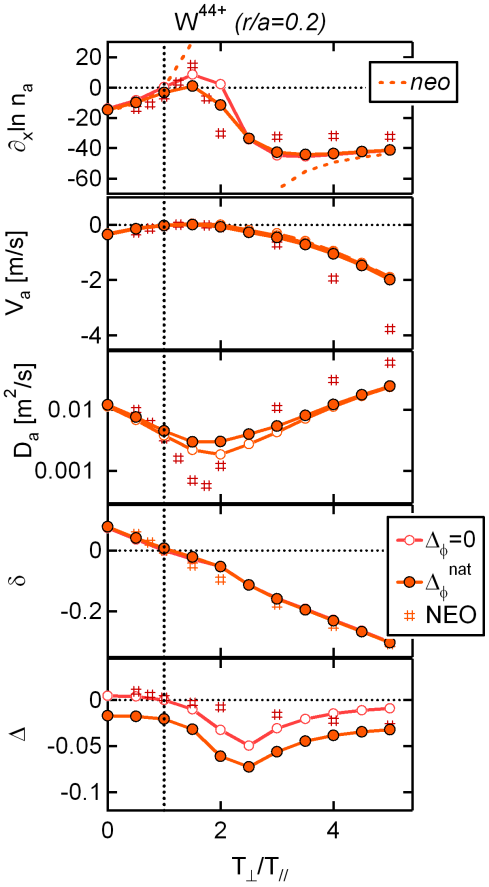

Figure 12. From top to bottom, as a function of the minority ion temperature anisotropy: Steady-state impurity peaking, pinch velocity, diffusion coefficient, horizontal and vertical asymmetries at $r/a = 0.2$ for W^{44+}, with $\Delta_\phi = 0$ and $\Delta_\phi = \Delta_\phi^{nat}$. The steady state peaking obtained by cancelling only the neoclassical flux is also indicated ("neo"), and the results from NEO are shown with hashtags symbols.

range where the impurity is expelled should lead however to an abrupt transition to a regime of strong accumulation that has not been encountered (or documented) so far in experiments. An empirical estimate of this critical value, indicated by a large red dashed line in figure 14, is

$$\left(T_\perp/T_\parallel\right)^{crit} \approx 2\left[1+\frac{M_i^2}{f_H}\left(\frac{m_a}{m_i}\frac{Z_i+T_i/T_e}{Z_a}\right)\right] \tag{56}$$

4. Conclusion

We have derived in this paper a simplified analytic formulation of the self-consistent problem of poloidal impurity distribution and radial flux in the Pfirsh-Schlüter regime, covering the effect of anisotropic electrostatic potential and of toroidal rotation. This work extends earlier finding that the poloidal distribution can be formulated

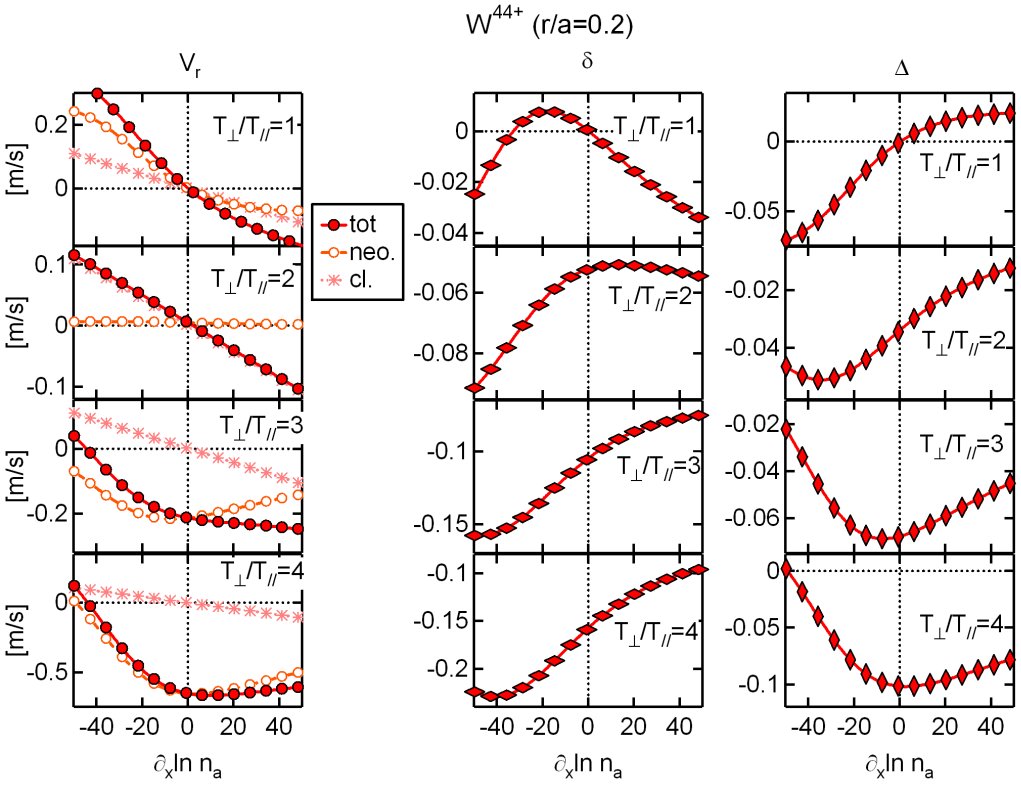

Figure 13. Total, neoclassical and classical impurity flux (left), horizontal (middle) and vertical (right) asymmetries as a function of the impurity peaking for different values of the minority ion temperature anisotropy, for W^{44+} at $r/a = 0.2$ ($\Delta_\phi = 0$).

in a geometric representation [Maget et al., 2020]. The poloidal asymmetry varies in particular with the impurity gradient via the combination of the diamagnetic velocity and the friction force, and therefore differs in transient and steady states. Three applications of experimental interest ("natural" case, toroidal rotation and ICRH heating) have been considered, and the predictions of the model have been compared with earlier works applicable to a flat impurity profile [Helander, 1998, Fülöp and Helander, 1999], and with computations of the steady state using the NEO code [Belli and Candy, 2008]. These comparisons validate our model in their distinct application domains (flat impurity profile and steady state respectively).

Focusing on the benchmark against NEO, we reported a satisfactory agreement with the diffusion, pinch velocity and poloidal asymmetry of Tungsten for a toroidal plasma rotation raising up to a ion Mach number of about 0.3. Regarding ICRH heating, a good agreement with the Tungsten peaking is found, although both diffusion and pinch velocity are underestimated above $T_\perp/T_\parallel \sim 3$. The equilibrium Tungsten profile tends to be flat or hollow at moderate temperature anisotropy, reflecting the beneficial effect of ICRH heating reported in experimental observation. But both our model and NEO are predicting a strong accumulation above some critical value, for which we propose an empirical formulae. To our knowledge, this situation has not been

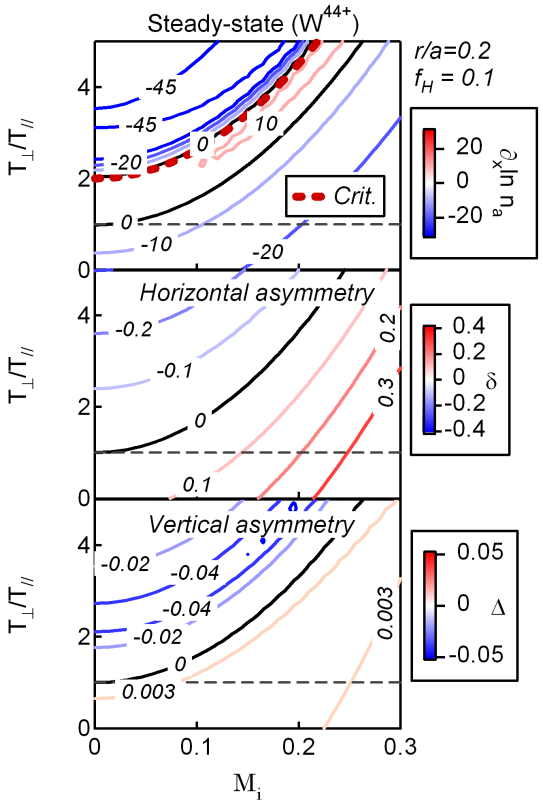

Figure 14. From top to bottom: steady state W^{44+} peaking, horizontal and vertical asymmetry, as a function of the ion Mach number and of the minority ion temperature anisotropy, at $r/a = 0.2$ and with $\Delta_\phi = 0$. The isotropic case $T_\perp/T_\parallel = 1$ is indicated by a dashed line ($\Delta_\phi = 0$), and the empirical estimate $\left(T_\perp/T_\parallel\right)^{crit}$ by the red dashed line.

reported so far in experimental analyses. The reason may be that this accumulation is compensated, fully or partly, by additional thermal screening from the minority species [Casson et al., 2015], not considered here, or that toroidal rotation is always sufficiently strong to push this situation outside the accessible range in experiments. Another interesting result found when applying the model to ICRH heating is that retaining the classical flux in addition to the neoclassical one can be important for determining the steady-state impurity gradient in particular ranges of parameters where the neoclassical diffusion coefficient can be nearly suppressed by the self-consistent poloidal asymmetry of the impurity.

In the natural case (no toroidal rotation and no ICRH heating), we have shown that even a small residual asymmetry of the electrostatic potential can considerably change the impurity peaking. This sensitivity has been evidenced here with respect to the positive vertical asymmetry of the electrostatic potential driven by collisions. It is proportional to the ion temperature gradient and drives an inward pinch. The amplitude found with NEO for this asymmetry is consistent with theory, and we note

that a significant contribution of the electrostatic potential asymmetry to the poloidal distribution of highly charged impurities was also outlined in PIC simulations with the XGCa code [Dominski et al., 2019]. The amplitude of this effect decreases at low collisionality, and becomes subdominant as soon as a sufficiently large external source of poloidal asymmetry is considered, for example, when the ion Mach number exceeds few percents. Note that it adds to the turbulence driven asymmetry of the electrostatic potential that also generates an asymmetry of the impurity distribution [Estève et al., 2018]. This "natural" case appears as the most critical in the benchmark against NEO. The friction force between the impurity and the main ions plays a large role in the poloidal distribution, and transfers the vertical asymmetry of the electrostatic potential in a combination of vertical and horizontal asymmetries of the impurity. This transfer is not recovered in NEO, possibly because of the ordering assumptions made in the code.

The model described in this paper, being able to describe transient situations where the impurity is still evolving towards steady state, can be of interest for integrated simulation purposes, where the time scale of collisional transport competes with turbulent one, as well as with the dynamics of radiation losses and equilibrium evolution. Its formulation allows a fast computation (by 6 orders of magnitude compared with NEO) although the geometrical simplifications (circular plasmas) and collisional range of application limits its accuracy in its present form.

Acknowledgments

This work has been carried out within the framework of the French Research Federation for Fusion Studies, and of the EUROfusion Consortium. It has received funding from the Euratom research and training programme 2014-2018 and 2019-2020 under grant agreement No 633053 for the project ENR-MFE19.CEA-03. The views and opinions expressed herein do not necessarily reflect those of the European Commission.

References

[Angioni and Helander, 2014] Angioni, C. and Helander, P. (2014). Neoclassical transport of heavy impurities with poloidally asymmetric density distribution in tokamaks. *Plasma Physics and Controlled Fusion*, 56(12):124001, http://stacks.iop.org/0741-3335/56/i=12/a=124001.

[Angioni et al., 2014] Angioni, C., Mantica, P., Pütterich, T., Valisa, M., Baruzzo, M., Belli, E., Belo, P., Casson, F., Challis, C., Drewelow, P., Giroud, C., Hawkes, N., Hender, T., Hobirk, J., Koskela, T., Taroni, L. L., Maggi, C., Mlynar, J., Odstrcil, T., Reinke, M., Romanelli, M., and Contributors, J. E. (2014). Tungsten transport in JET H-mode plasmas in hybrid scenario, experimental observations and modelling. *Nuclear Fusion*, 54(8):083028, http://stacks.iop.org/0029-5515/54/i=8/a=083028.

[Belli and Candy, 2008] Belli, E. A. and Candy, J. (2008). Kinetic calculation of neoclassical transport including self-consistent electron and impurity dynamics. *Plasma Physics and Controlled Fusion*, 50(9):095010, DOI: 10.1088/0741-3335/50/9/095010, https://doi.org/10.1088%2F0741-3335%2F50%2F9%2F095010.

[Belli et al., 2014] Belli, E. A., Candy, J., and Angioni, C. (2014). Pfirsch-schlter neoclassical heavy impurity transport in a rotating plasma. *Plasma Physics and Controlled Fusion*, 56(12):124002, DOI: 10.1088/0741-3335/56/12/124002, https://doi.org/10.1088%2F0741-3335%2F56%2F12%2F124002.

[Bilato et al., 2014] Bilato, R., Maj, O., and Angioni, C. (2014). Modelling the influence of temperature anisotropies on poloidal asymmetries of density in the core of rotating plasmas. *Nuclear Fusion*, 54(7):072003, DOI: 10.1088/0029-5515/54/7/072003, https://doi.org/10.1088%2F0029-5515%2F54%2F7%2F072003.

[Bilato et al., 2017] Bilato, R., Odstrcil, T., Casson, F., Angioni, C., Brambilla, M., Kazakov, Y., and Poli, E. (2017). The impact of the ion-cyclotron-resonance location on the poloidal asymmetries of impurity density in an ICRF-heated rotating plasma. *Nuclear Fusion*, 57(5):056020, DOI: 10.1088/1741-4326/aa5fd6, https://doi.org/10.1088%2F1741-4326%2Faa5fd6.

[Bourdelle et al., 2015] Bourdelle, C., Artaud, J., Basiuk, V., Bécoulet, M., Brémond, S., Bucalossi, J., Bufferand, H., Ciraolo, G., Colas, L., Corre, Y., Courtois, X., Decker, J., Delpech, L., Devynck, P., Dif-Pradalier, G., Doerner, R., Douai, D., Dumont, R., Ekedahl, A., Fedorczak, N., Fenzi, C., Firdaouss, M., Garcia, J., Ghendrih, P., Gil, C., Giruzzi, G., Goniche, M., Grisolia, C., Grosman, A., Guilhem, D., Guirlet, R., Gunn, J., Hennequin, P., Hillairet, J., Hoang, T., Imbeaux, F., Ivanova-Stanik, I., Joffrin, E., Kallenbach, A., Linke, J., Loarer, T., Lotte, P., Maget, P., Marandet, Y., Mayoral, M., Meyer, O., Missirlian, M., Mollard, P., Monier-Garbet, P., Moreau, P., Nardon, E., Pégourié, B., Peysson, Y., Sabot, R., Saint-Laurent, F., Schneider, M., Travère, J., Tsitrone, E., Vartanian, S., Vermare, L., Yoshida, M., and and, R. Z. (2015). WEST physics basis. *Nuclear Fusion*, 55(6):063017, DOI: 10.1088/0029-5515/55/6/063017, https://doi.org/10.1088%2F0029-5515%2F55%2F6%2F063017.

[Casson et al., 2015] Casson, F. J., Angioni, C., Belli, E. A., Bilato, R., Mantica, P., Odstrcil, T., Pütterich, T., Valisa, M., Garzotti, L., Giroud, C., Hobirk, J., Maggi, C. F., Mlynar, J., and Reinke, M. L. (2015). Theoretical description of heavy impurity transport and its application to the modelling of tungsten in JET and ASDEX upgrade. *Plasma Physics and Controlled Fusion*, 57(1):014031, DOI: 10.1088/0741-3335/57/1/014031, https://doi.org/10.1088%2F0741-3335%2F57%2F1%2F014031.

[Chan et al., 1985] Chan, V., Chiu, S., and Wong, S. (1985). Impurity transport in ICRH tokamak plasma. *Nuclear Fusion*, 25(6):697–704, DOI: 10.1088/0029-5515/25/6/004, https://doi.org/10.1088%2F0029-5515%2F25%2F6%2F004.

[Dominski et al., 2019] Dominski, J., Chang, C. S., Hager, R., Helander, P., Ku, S., and Yoon, E. S. (2019). Study of updown poloidal density asymmetry of high- Z impurities with the new impurity version of XGCa. *Journal of Plasma Physics*, 85(5):905850510, DOI: 10.1017/S0022377819000722.

[Donnel et al., 2018] Donnel, P., Garbet, X., Sarazin, Y., Asahi, Y., Wilczynski, F., Caschera, E., Dif-Pradalier, G., Ghendrih, P., and Gillot, C. (2018). Turbulent generation of poloidal asymmetries of the electric potential in a tokamak. *Plasma Physics and Controlled Fusion*, 61(1):014003, DOI: 10.1088/1361-6587/aae4fe, https://doi.org/10.1088%2F1361-6587%2Faae4fe.

[Donnel et al., 2019] Donnel, P., Garbet, X., Sarazin, Y., Grandgirard, V., Bouzat, N., Caschera, E., Dif-Pradalier, G., Ghendrih, P., Gillot, C., Latu, G., and Passeron, C. (2019). Neoclassical impurity flux in presence of turbulent generated poloidal asymmetries and pressure anisotropy. *Plasma Physics and Controlled Fusion*, 61(4):044006, DOI: 10.1088/1361-6587/ab04b8, https://doi.org/10.1088%2F1361-6587%2Fab04b8.

[Efthimion et al., 1999] Efthimion, P., Goeler, S. V., Houlberg, W., Synakowski, E., Zarnstorff, M., Batha, S., Bell, R., Bitter, M., Bush, C., Levinton, F., Mazzucato, E., McCune, D., Mueller, D., Park, H., Ramsey, A., Roquemore, A., and Taylor, G. (1999). Observation of neoclassical transport in reverse shear plasmas on TFTR. *Nuclear Fusion*, 39(11Y):1905–1909, DOI: 10.1088/0029-5515/39/11y/333, https://doi.org/10.1088%2F0029-5515%2F39%2F11y%2F333.

[Estève et al., 2018] Estève, D., Sarazin, Y., Garbet, X., Grandgirard, V., Breton, S., Donnel, P., Asahi, Y., Bourdelle, C., Dif-Pradalier, G., Ehrlacher, C., Emeriau, C., Ghendrih, P., Gillot, C., Latu, G., and Passeron, C. (2018). Self-consistent gyrokinetic modeling of neoclassical and turbulent impurity transport. *Nuclear Fusion*, 58(3):036013, http://stacks.iop.org/0029-5515/58/i=3/a=036013.

[Fedorczak et al., 2015] Fedorczak, N., Monier-Garbet, P., Pütterich, T., Brezinsek, S., Devynck, P., Dumont, R., Goniche, M., Joffrin, E., Lerche, E., Lipschultz, B., de la Luna, E., Maddison, G., Maggi, C., Matthews, G., Nunes, I., Rimini, F., Solano, E., Tamain, P., Tsalas, M., and de Vries, P. (2015). Tungsten transport and sources control in JET ITER-like wall H-mode plasmas. *Journal of Nuclear Materials*, 463:85 – 90, ISSN: 0022-3115, DOI: https://doi.org/10.1016/j.jnucmat.2014.12.044, http://www.sciencedirect.com/science/article/pii/S0022311514009866. PLASMA-SURFACE INTERACTIONS 21.

[Fülöp and Helander, 1999] Fülöp, T. and Helander, P. (1999). Nonlinear neoclassical transport in a rotating impure plasma with large gradients. *Physics of Plasmas*, 6(8):3066–3075, DOI: 10.1063/1.873593, https://doi.org/10.1063/1.873593.

[Goniche et al., 2017] Goniche, M., Dumont, R. J., Bobkov, V., Buratti, P., Brezinsek, S., Challis, C., Colas, L., Czarnecka, A., Drewelow, P., Fedorczak, N., Garcia, J., Giroud, C., Graham, M., Graves, J. P., Hobirk, J., Jacquet, P., Lerche, E., Mantica, P., Monakhov, I., Monier-Garbet, P., Nave, M. F. F., Noble, C., Nunes, I., Ptterich, T., Rimini, F., Sertoli, M., Valisa, M., and and, D. V. E. (2017). Ion cyclotron resonance heating for tungsten control in various JET h-mode scenarios. *Plasma Physics and Controlled Fusion*, 59(5):055001, DOI: 10.1088/1361-6587/aa60d2, https://doi.org/10.1088%2F1361-6587%2Faa60d2.

[Guirlet et al., 2006] Guirlet, R., Giroud, C., Parisot, T., Puiatti, M. E., Bourdelle, C., Carraro, L., Dubuit, N., Garbet, X., and Thomas, P. R. (2006). Parametric dependences of impurity transport in tokamaks. *Plasma Physics and Controlled Fusion*, 48(12B):B63–B74, DOI: 10.1088/0741-3335/48/12b/s06, https://doi.org/10.1088%2F0741-3335%2F48%2F12b%2Fs06.

[Helander, 1998] Helander, P. (1998). Bifurcated neoclassical particle transport. *Physics of Plasmas*, 5(11):3999–4004, DOI: 10.1063/1.873121, https://doi.org/10.1063/1.873121.

[Hinton and Rosenbluth, 1973] Hinton, F. L. and Rosenbluth, M. N. (1973). Transport properties of a toroidal plasma at low to intermediate collision frequencies. *The Physics of Fluids*, 16(6):836–854, DOI: 10.1063/1.1694436, https://aip.scitation.org/doi/abs/10.1063/1.1694436.

[Ida et al., 1987] Ida, K., Fonck, R. J., Sesnic, S., Hulse, R. A., and LeBlanc, B. (1987). Observation of z-dependent impurity accumulation in the PBX tokamak. *Phys. Rev. Lett.*, 58:116–119, DOI: 10.1103/PhysRevLett.58.116, https://link.aps.org/doi/10.1103/PhysRevLett.58.116.

[Ingesson et al., 2000] Ingesson, L. C., Chen, H., Helander, P., and Mantsinen, M. J. (2000). Comparison of basis functions in soft x-ray tomography and observation of poloidal asymmetries in impurity density. *Plasma Physics and Controlled Fusion*, 42(2):161–180, DOI: 10.1088/0741-3335/42/2/308, https://doi.org/10.1088%2F0741-3335%2F42%2F2%2F308.

[Kazakov et al., 2012] Kazakov, Y. O., Pusztai, I., Fülp, T., and Johnson, T. (2012). Poloidal asymmetries due to ion cyclotron resonance heating. *Plasma Physics and Controlled Fusion*, 54(10):105010, DOI: 10.1088/0741-3335/54/10/105010, https://doi.org/10.1088%2F0741-3335%2F54%2F10%2F105010.

[Kessel, 1994] Kessel, C. (1994). Bootstrap current in a tokamak. *Nucl. Fusion*, 34(9):1221–1238.

[Maget et al., 2020] Maget, P., Frank, J., Nicolas, T., Agullo, O., Garbet, X., and Lütjens, H. (2020). Natural poloidal asymmetry and neoclassical transport of impurities in tokamak plasmas. *Plasma Physics and Controlled Fusion*, 62(2):025001, DOI: 10.1088/1361-6587/ab53ab, https://doi.org/10.1088%2F1361-6587%2Fab53ab.

[Neu et al., 2002] Neu, R., Dux, R., Geier, A., Kallenbach, A., Pugno, R., Rohde, V., Bolshukhin, D., Fuchs, J. C., Gehre, O., Gruber, O., Hobirk, J., Kaufmann, M., Krieger, K., Laux, M., Maggi, C., Murmann, H., Neuhauser, J., Ryter, F., Sips, A. C. C., Stbler, A., Stober, J., Suttrop, W.,

Zohm, H., and the ASDEX Upgrade Team (2002). Impurity behaviour in the ASDEX Upgrade divertor tokamak with large area tungsten walls. *Plasma Physics and Controlled Fusion*, 44(6):811–826, DOI: 10.1088/0741-3335/44/6/313, https://doi.org/10.1088%2F0741-3335%2F44%2F6%2F313.

[Parisot et al., 2008] Parisot, T., Guirlet, R., Bourdelle, C., Garbet, X., Dubuit, N., Imbeaux, F., and Thomas, P. R. (2008). Experimental impurity transport and theoretical interpretation in a Tore Supra lower-hybrid heated plasma. *Plasma Physics and Controlled Fusion*, 50(5):055010, DOI: 10.1088/0741-3335/50/5/055010, https://doi.org/10.1088%2F0741-3335%2F50%2F5%2F055010.

[Pedersen et al., 2000] Pedersen, T. S., Granetz, R., Hubbard, A., Hutchinson, I., Marmar, E., Rice, J., and Terry, J. (2000). Radial impurity transport in the H mode transport barrier region in Alcator C-Mod. *Nuclear Fusion*, 40(10):1795–1804, DOI: 10.1088/0029-5515/40/10/310, https://doi.org/10.1088%2F0029-5515%2F40%2F10%2F310.

[Petrasso et al., 1986] Petrasso, R. D., Sigmar, D. J., Wenzel, K. W., Hopf, J. E., Greenwald, M., Terry, J. L., and Parker, J. (1986). Observations of Centrally Peaked Impurity Profiles Following Pellet Injection in the Alcator-C Tokamak. *Phys. Rev. Lett.*, 57:707–710, DOI: 10.1103/PhysRevLett.57.707, https://link.aps.org/doi/10.1103/PhysRevLett.57.707.

[Pütterich et al., 2011] Pütterich, T., Dux, R., Janzer, M., and McDermott, R. (2011). ELM flushing and impurity transport in the H-mode edge barrier in ASDEX Upgrade. *Journal of Nuclear Materials*, 415(1, Supplement):S334 – S339, ISSN: 0022-3115, DOI: https://doi.org/10.1016/j.jnucmat.2010.09.052, http://www.sciencedirect.com/science/article/pii/S0022311510005623. Proceedings of the 19th International Conference on Plasma-Surface Interactions in Controlled Fusion.

[Rapp et al., 1997] Rapp, J., Tokar, M. Z., Knen, L., Koslowski, H. R., Bertschinger, G., Brix, M., Claassen, H., Jaspers, R., Krmer-Flecken, A., Ohya, K., Philipps, V., Pospieszczyk, A., Samm, U., Tanabe, T., Telesca, G., Unterberg, B., and Oost, G. V. (1997). Transport studies of high-zelements in neon edge radiation cooled discharges in TEXTOR-94. *Plasma Physics and Controlled Fusion*, 39(10):1615–1634, DOI: 10.1088/0741-3335/39/10/009, https://doi.org/10.1088%2F0741-3335%2F39%2F10%2F009.

[Reinke et al., 2012] Reinke, M. L., Hutchinson, I. H., Rice, J. E., Howard, N. T., Bader, A., Wukitch, S., Lin, Y., Pace, D. C., Hubbard, A., Hughes, J. W., and Podpaly, Y. (2012). Poloidal variation of high-Zimpurity density due to hydrogen minority ion cyclotron resonance heating on Alcator C-Mod. *Plasma Physics and Controlled Fusion*, 54(4):045004, DOI: 10.1088/0741-3335/54/4/045004, https://doi.org/10.1088%2F0741-3335%2F54%2F4%2F045004.

[Rice et al., 2002] Rice, J., Bonoli, P., Marmar, E., Wukitch, S., Boivin, R., Fiore, C., Granetz, R., Greenwald, M., Hubbard, A., Hughes, J., Hutchinson, I., Irby, J., Lin, Y., Mossessian, D., Porkolab, M., Schilling, G., Snipes, J., and Wolfe, S. (2002). Double transport barrier plasmas in Alcator C-Mod. *Nuclear Fusion*, 42(5):510–519, DOI: 10.1088/0029-5515/42/5/303, https://doi.org/10.1088%2F0029-5515%2F42%2F5%2F303.

[Rice et al., 1997] Rice, J. E., Terry, J. L., Goetz, J. A., Wang, Y., Marmar, E. S., Greenwald, M., Hutchinson, I., Takase, Y., Wolfe, S., Ohkawa, H., and Hubbard, A. (1997). Impurity transport in Alcator C-Mod plasmas. *Physics of Plasmas*, 4(5):1605–1609, DOI: 10.1063/1.872291, https://doi.org/10.1063/1.872291.

[Romanelli and Ottaviani, 1998] Romanelli, M. and Ottaviani, M. (1998). Effects of density asymmetries on heavy impurity transport in a rotating tokamak plasma. *Plasma Physics and Controlled Fusion*, 40(10):1767–1773, DOI: 10.1088/0741-3335/40/10/007, https://doi.org/10.1088%2F0741-3335%2F40%2F10%2F007.

[Tokar et al., 1995] Tokar, M. Z., Baelmans, T., Philipps, V., Reiter, D., Samm, U., Unterberg, B., Classen, H. A., Gerhauser, H., Hey, J. D., Huber, A., Mertens, P., Lie, Y. T., Ongena, J., Pospieszczyk, A., Putz, T., Rapp, J., Rusbuld, D., Schorn, R. P., and Schweer, B. (1995).

The influence of impurities on limiter tokamak plasmas and relevant mechanisms. *Plasma Physics and Controlled Fusion*, 37(11A):A241–A253, DOI: 10.1088/0741-3335/37/11a/016, https://doi.org/10.1088%2F0741-3335%2F37%2F11a%2F016.

[Valisa et al., 2011] Valisa, M., Carraro, L., Predebon, I., Puiatti, M., Angioni, C., Coffey, I., Giroud, C., Taroni, L. L., Alper, B., Baruzzo, M., daSilva, P. B., Buratti, P., Garzotti, L., Eester, D. V., Lerche, E., Mantica, P., Naulin, V., Tala, T., and and, M. T. (2011). Metal impurity transport control in JET H-mode plasmas with central ion cyclotron radiofrequency power injection. *Nuclear Fusion*, 51(3):033002, DOI: 10.1088/0029-5515/51/3/033002, https://doi.org/10.1088%2F0029-5515%2F51%2F3%2F033002.

[Villegas et al., 2010] Villegas, D., Guirlet, R., Bourdelle, C., Hoang, G. T., Garbet, X., and Sabot, R. (2010). Experimental electron temperature gradient dependence of heavy impurity transport in fusion devices. *Phys. Rev. Lett.*, 105:035002, DOI: 10.1103/PhysRevLett.105.035002, https://link.aps.org/doi/10.1103/PhysRevLett.105.035002.

[Wong and Chan, 2009] Wong, S. K. and Chan, V. S. (2009). Self-consistent poloidal electric field and neoclassical angular momentum flux. *Physics of Plasmas*, 16(12):122507, DOI: 10.1063/1.3278597, https://doi.org/10.1063/1.3278597.

Appendix A. Derivation

The derivation of the model follows closely the one without toroidal rotation described in [Maget et al., 2020]. We consider an axisymmetric equilibrium with a magnetic field expressed as $\mathbf{B} = F\nabla\varphi + \nabla\varphi \times \nabla\psi$ and $J^{-1} = \nabla\psi \cdot \nabla\theta \times \nabla\varphi$. The steady state momentum equation of a species 'a' of fluid velocity $\mathbf{V_a}$ writes:

$$-\frac{m_a n_a \Omega^2}{2}\nabla R^2 = -\nabla p_a + n_a e_a \left(\mathbf{E} + \mathbf{V_a} \times \mathbf{B}\right) + \mathbf{R_a} \tag{A.1}$$

where $\mathbf{R_a}$ is the friction force, and the inertial term on the LHS has been simplified by considering a pure rigid toroidal rotation of angular frequency Ω. We neglect in this analysis the neoclassical viscous tensor, which means that the impurity is assumed to be in the Pfirsh-Schlüter regime. The scalar product of equation (A.1) with $R^2\nabla\varphi$ gives the radial particle flux:

$$\Gamma_a \cdot \nabla\psi = -n_a \mathbf{E} \cdot R^2\nabla\varphi - \frac{\mathbf{R_a}}{e_a} \cdot R^2\nabla\varphi \tag{A.2}$$

and using the relation :

$$R^2\nabla\varphi = \frac{F}{B^2}\mathbf{B} - \frac{\mathbf{B} \times \nabla\psi}{B^2} \tag{A.3}$$

we obtain:

$$\Gamma_a \cdot \nabla\psi = -n_a \frac{F}{B^2}\left(\mathbf{E} \cdot \mathbf{B} + \frac{\mathbf{R_a} \cdot \mathbf{B}}{e_a n_a}\right) + \frac{\mathbf{R_a}}{e_a} \cdot \frac{\mathbf{B} \times \nabla\psi}{B^2} + n_a \mathbf{E} \cdot \frac{\mathbf{B} \times \nabla\psi}{B^2} \tag{A.4}$$

where we have, using $\mathbf{E} \equiv -\nabla\phi$ (we neglect $\partial_t\psi$):

$$\mathbf{E} \cdot \frac{\mathbf{B} \times \nabla\psi}{B^2} = -\frac{F}{JB^2}\partial_\theta\phi \tag{A.5}$$

The projection parallel to $\mathbf{B}$ of equation (A.1) gives, using $J \equiv 1/\mathbf{B} \cdot \nabla\theta$:

$$\mathbf{E} \cdot \mathbf{B} + \frac{\mathbf{R_a} \cdot \mathbf{B}}{e_a n_a} = \frac{1}{J}\left(\frac{\partial_\theta p_a}{e_a n_a} - \frac{m_a \Omega^2}{2e_a}\partial_\theta R^2\right) \tag{A.6}$$

which, injected into equation (A.4) gives:

$$\Gamma_a \cdot \nabla\psi = -\frac{F}{e_a J B^2}\left(\partial_\theta p_a + e_a n_a \partial_\theta \phi - \frac{m_a n_a \Omega^2}{2}\partial_\theta R^2\right) + \frac{\mathbf{R_a}}{e_a}\cdot\frac{\mathbf{B}\times\nabla\psi}{B^2} \tag{A.7}$$

The first term is the neoclassical flux and the second one is the classical flux.

Appendix A.1. Neoclassical flux

From equation (A.6) we get:

$$R_{a\parallel} = \frac{n_a T_a}{JB}\left[\frac{\partial_\theta p_a}{n_a T_a} + \frac{e_a}{T_a}\partial_\theta\phi - \frac{m_a\Omega^2}{2T_a}\partial_\theta R^2\right] \tag{A.8}$$

so that equation (A.7) becomes:

$$\Gamma_a^{neo}\cdot\nabla\psi = -\frac{F}{e_a B}R_{a\parallel} \tag{A.9}$$

The parallel friction can be expressed as:

$$R_{a\parallel} = -n_a m_a \nu_a\left(V_{a\parallel} - V_{i\parallel} + C_0^a\frac{2q_{\parallel i}}{5p_i}\right) \tag{A.10}$$

$$C_0^a = \frac{3}{2}\frac{1}{1+\frac{T_a}{T_i}\frac{m_i}{m_a}} \tag{A.11}$$

The assumption of stationarity $\nabla\cdot(n_a\mathbf{V_a}) = 0$ gives

$$\frac{1}{J}\partial_\psi\left(Jn_a\mathbf{V_a}\cdot\nabla\psi\right) + \frac{1}{J}\partial_\theta\left(Jn_a\mathbf{V_a}\cdot\nabla\theta\right) + \frac{1}{J}\partial_\varphi\left(Jn_a\mathbf{V_a}\cdot\nabla\varphi\right) = 0 \tag{A.12}$$

We assume that the first term is negligible. This is justified whenever the radial component of the velocity is small compared with its poloidal component. In the axisymmetric case ($\partial_\varphi = 0$) we then have :

$$\frac{\mathbf{V_a}\cdot\nabla\theta}{\mathbf{B}\cdot\nabla\theta} = \frac{K_a(\psi)}{n_a} \tag{A.13}$$

where $K_a(\psi)$ is an unknown function.

From equation (A.1), the fluid velocity can be expressed as:

$$\mathbf{V_a} = \frac{V_{a\parallel}}{B}\mathbf{B} + \frac{T_a}{e_a}A_a\frac{\mathbf{B}\times\nabla\psi}{B^2} + \frac{T_a}{e_a}A_a^\theta\frac{\mathbf{B}\times\nabla\theta}{B^2} \tag{A.14}$$

where

$$A_a = \partial_\psi \ln p_a + (e_a/T_a)\partial_\psi\phi - m_a\Omega^2/(2T_a)\partial_\psi R^2 \tag{A.15}$$

$$A_a^\theta = \partial_\theta \ln p_a + (e_a/T_a)\partial_\theta\phi - m_a\Omega^2/(2T_a)\partial_\theta R^2 \tag{A.16}$$

From the expression of $\mathbf{V_a}$ we obtain

$$\frac{\mathbf{V_a}\cdot\nabla\theta}{\mathbf{B}\cdot\nabla\theta} = \frac{V_{a\parallel}}{B} + \frac{F}{B^2}\frac{T_a}{e_a}A_a \tag{A.17}$$

This gives using equation (A.13):

$$V_{a\parallel} = \frac{K_a(\psi)}{n_a}B - \frac{T_a}{e_a}A_a\frac{F}{B} \tag{A.18}$$

Similarly for the main ion parallel heat flux, using $\nabla \cdot \mathbf{q_i} = 0$ and $q_{\perp,i} = \frac{5}{2} p_i \mathbf{V^*_{Ti}}$ with $\mathbf{V^*_{Ti}} = (\mathbf{B} \times \nabla T_i)/(e_i B^2)$, we can write:

$$q_{i\parallel} = L_i(\psi) B - \frac{5}{2} \frac{p_i}{e_i} \frac{F}{B} \partial_\psi T_i \tag{A.19}$$

Using the notation $u_{2\parallel i} = 2 q_{i\parallel} B/(5 p_i)$ we can write

$$\begin{aligned} u_{2\parallel i} &= \frac{2 L_i(\psi)}{5 \langle n_i \rangle T_i} \frac{B^2}{N} - F \frac{\partial_\psi T_i}{e_i} \\ &= \langle u_{2\parallel i} \rangle \frac{B^2/N}{\langle B^2/N \rangle} + \left(\frac{B^2/N}{\langle B^2/N \rangle} - 1 \right) F \frac{\partial_\psi T_i}{e_i} \end{aligned} \tag{A.20}$$

with $N = n_i / \langle n_i \rangle$, and we define :

$$u(\psi) = \frac{K_i(\psi)}{\langle n_i \rangle} - \frac{C_0^a}{\langle B^2/N \rangle} \left(F \frac{\partial_\psi T_i}{e_i} + \langle u_{2\parallel i} \rangle \right) \tag{A.21}$$

This gives

$$\frac{R_{a\parallel}}{n_a m_a \nu_a} = \frac{F}{B} \left(\frac{T_a}{e_a} A_a - \frac{T_i}{e_i} A_i + C_0^a \frac{\partial_\psi T_i}{e_i} \right) - \frac{K_a}{n_a} B + u(\psi) \frac{B}{N} \tag{A.22}$$

At equilibrium, since the surface average cancels the operator $(\mathbf{B} \cdot \nabla)$, we have (assuming isothermal flux surfaces):

$$T_a \langle B \nabla_\parallel \ln n_a \rangle + e_a \langle B \nabla_\parallel \phi \rangle - \frac{m_a \Omega^2}{2} \langle B \nabla_\parallel R^2 \rangle = 0 \tag{A.23}$$

so that $\langle B R_{a\parallel}/n_a \rangle = 0$, and using equation (A.10) we obtain:

$$K_a \left\langle \frac{B^2}{n_a} \right\rangle - K_i \left\langle \frac{B^2}{n_i} \right\rangle + C_0^a \langle u_{2\parallel i} \rangle - F \frac{T_a}{e_a} \langle A_a \rangle + F \frac{T_i}{e_i} \langle A_i \rangle = 0 \tag{A.24}$$

This gives, using equations (A.21) and (A.24) to eliminate K_i and K_a:

$$\begin{aligned} \frac{R_{a\parallel}}{n_a m_a \nu_a} = \frac{F}{B} \frac{T_a}{e_a} \Bigg[& \mathcal{G}_\psi \left(1 - \frac{b^2/n}{\langle b^2/n \rangle} \right) + \mathcal{U}_\psi \left\langle \frac{b^2}{N} \right\rangle \left(\frac{b^2/N}{\langle b^2/N \rangle} - \frac{b^2/n}{\langle b^2/n \rangle} \right) \\ & + \frac{m_a \Omega^2}{2 T_a} \left(1 - \frac{m_i}{m_a} \frac{e_a}{e_i} \right) \left(\frac{b^2/n}{\langle b^2/n \rangle} \langle \partial_\psi R^2 \rangle - \partial_\psi R^2 \right) \Bigg] \end{aligned} \tag{A.25}$$

with

$$\mathcal{G}_\psi \equiv \partial_\psi \ln p_a - \frac{T_i}{T_a} \frac{e_a}{e_i} \partial_\psi \ln p_i + C_0^a \frac{T_i}{T_a} \frac{e_a}{e_i} \partial_\psi \ln T_i \tag{A.26}$$

$$\mathcal{U}_\psi \equiv u(\psi) \frac{\langle B^2 \rangle}{F} \frac{e_a}{T_a} \tag{A.27}$$

The surface average neoclassical flux can then be derived from equation (A.9):

$$\begin{aligned} \langle \Gamma_a^{neo} \cdot \nabla \psi \rangle = m_a \nu_a \langle n_a \rangle \frac{F^2 T_a}{e_a^2 \langle B^2 \rangle} \Bigg[& \left(\frac{1}{\left\langle \frac{b^2}{n} \right\rangle} - \left\langle \frac{n}{b^2} \right\rangle \right) \mathcal{G}_\psi + \left(\frac{\langle b^2/N \rangle}{\langle b^2/n \rangle} - \left\langle \frac{n}{N} \right\rangle \right) \mathcal{U}_\psi \\ & + \frac{m_a \Omega^2}{2 T_a} \left(1 - \frac{m_i}{m_a} \frac{e_a}{e_i} \right) \left(\left\langle \frac{n \partial_\psi R^2}{b^2} \right\rangle - \frac{\langle \partial_\psi R^2 \rangle}{\langle b^2/n \rangle} \right) \Bigg] \end{aligned} \tag{A.28}$$

Appendix A.2. Classical flux

The classical flux can be calculated from:

$$R_{a\perp} = -n_a m_a \nu_a \left(\mathbf{V_{a\perp}} - \mathbf{V_{i\perp}} + C_a^0 \mathbf{V_{Ti}}\right) \tag{A.29}$$

This gives, using equation (A.14) in the simplified case where $\nabla\psi \cdot \nabla\theta \approx 0$:

$$\begin{aligned}\left\langle \Gamma_a^{cl} \cdot \nabla\psi \right\rangle \;=\; & -\frac{m_a \nu_a \left\langle n_a \right\rangle F^2 T_a}{e_a^2 \left\langle B^2 \right\rangle} \left[\left(\frac{\left\langle B^2 \right\rangle}{F^2} \left\langle n R^2 \right\rangle - \left\langle \frac{n}{b^2} \right\rangle \right) \mathcal{G}_\psi \right. \\ & \left. - \frac{m_a \Omega^2}{2T_a} \left(1 - \frac{m_i}{m_a}\frac{e_a}{e_i}\right) \left(\frac{\left\langle B^2 \right\rangle}{F^2} \left\langle n R^2 \partial_\psi R^2 \right\rangle - \left\langle \frac{n \partial_\psi R^2}{b^2} \right\rangle \right) \right]\end{aligned} \tag{A.30}$$

Appendix A.3. Poloidal asymmetry

The poloidal asymmetry can be obtained from equation (A.8) assuming isothermal flux surfaces:

$$\partial_\theta \ln n_a + \frac{e_a}{T_a}\partial_\theta \phi - \frac{m_a \Omega^2}{2T_a}\partial_\theta R^2 = JB \frac{R_{a\parallel}}{n_a T_a} \tag{A.31}$$

where

$$\begin{aligned}JB\frac{R_{a\parallel}}{n_a T_a} = \mathcal{A}_\psi \Bigg\{ & \left(1 - \frac{b^2/n}{\langle b^2/n \rangle}\right) \mathcal{G}_\psi + \left(\frac{b^2}{N} - \left\langle \frac{b^2}{N} \right\rangle \frac{b^2/n}{\langle b^2/n \rangle} \right) \mathcal{U}_\psi \\ & + \frac{m_a \Omega^2}{2T_a} \left(1 - \frac{m_i}{m_a}\frac{e_a}{e_i}\right) \left(\frac{b^2/n}{\langle b^2/n \rangle} \left\langle \partial_\psi R^2 \right\rangle - \partial_\psi R^2 \right) \Bigg\}\end{aligned} \tag{A.32}$$

with $\mathcal{A}_\psi = JF\, m_a \nu_a / e_a$.

Appendix B. Low aspect ratio

In the large aspect ratio limit we have:

$$\partial_\psi r = q/(rB_0) \tag{B.1}$$

The cos and sine components required for determining the poloidal asymmetry (equation A.32) are:

$$b^2/n \;= 1 - (2\epsilon + \delta)\cos\theta - \Delta \sin\theta \tag{B.2}$$

$$n/b^2 \;= 1 + (2\epsilon + \delta)\cos\theta + \Delta \sin\theta \tag{B.3}$$

$$\partial_r R^2 = r + 2R_0 \cos\theta \tag{B.4}$$

For the determination of the fluxes (equations A.28 and A.30), we use

$$R^2 \approx \frac{F^2}{B^2}\left[1 + \left(\frac{\epsilon}{q}\right)^2\right] \tag{B.5}$$

with $F \approx R_0 B_0$ to obtain

$$\left\langle n R^2 \right\rangle \;= \frac{R_0^2 B_0^2}{\left\langle B^2 \right\rangle} \left\langle \frac{n}{b^2} \right\rangle \left[1 + \left(\frac{\epsilon}{q}\right)^2\right] \tag{B.6}$$

$$\left\langle n R^2 \partial_r R^2 \right\rangle \;= \frac{R_0^2 B_0^2}{\left\langle B^2 \right\rangle} \left\langle \frac{n \partial_r R^2}{b^2} \right\rangle \left[1 + \left(\frac{\epsilon}{q}\right)^2\right] \tag{B.7}$$

We have also, following [Angioni and Helander, 2014]:

$$\left\langle b^2/n \right\rangle = 1 + \epsilon\delta + \frac{\delta^2 + \Delta^2}{2} \tag{B.8}$$

$$\left\langle n/b^2 \right\rangle = 1 + \epsilon\delta + 2\epsilon^2 \tag{B.9}$$

This gives

$$\left\langle \frac{n}{b^2}\partial_r R^2 \right\rangle - \frac{\langle \partial_r R^2 \rangle}{\langle b^2/n \rangle} \approx 2\epsilon R_0 \left(1 + \frac{\delta}{2\epsilon}\right) \tag{B.10}$$

$$\frac{\langle \partial_r R^2 \rangle}{\langle b^2/n \rangle}\frac{b^2}{n} - \partial_r R^2 \approx -R_0 \left(2\cos\theta + \epsilon\Delta \sin\theta\right) \tag{B.11}$$